

ABSTRACT

MEHTA, SHASHVAT TEJASKUMAR. Additive Manufacturing of Ultra-High Temperature Ceramic (UHTC) Composites using Electron Beam Melting Process. (Under the direction of Dr. Cheryl Xu).

Ultra-high temperature ceramic (UHTC) materials have been used in environments of extreme thermal loadings due to their high melting point and the unique ability to resist extreme thermal stresses in critical applications, such as the leading edges of hypersonic vehicles, aerospace re-entry vehicles, and rocket engines, etc. Traditional manufacturing processes restrict the freedom to manufacture parts with complex geometries due to the die and mold design limitations. Fully dense UHTC parts are difficult to produce with these processes due to their high melting point and low self-diffusivity. Electron Beam Melting (EB-PBF) process facilitates the manufacture of parts with complex properties and internal cavities by planned heating and melting of the powder bed attached layer-by-layer. In this research, an effort has been made to study the manufacture of UHTC-based materials using the EB-PBF process and to investigate the sintering ability of the manufactured samples under different processing conditions.

A Mathematical model was developed and simulated to computationally determine the optimized process parameters for ZrB_2 -30 vol% $ZrSi_2$ using EB-PBF. The mathematical model results were compared with the experimented observations and optimum process parameters are presented. For the combination of ZrB_2 -30 vol% $ZrSi_2$, the optimal process parameters are beam power of 500 W with scanning speeds of 500, 750, and 1000 mm/s; beam power of 1000 W with scanning speed of 1000 mm/s. The simulation results of the mathematical model lie within a close range of the experimented results and hence is a useful resource for future research experiments. The results of this study provide a new method to produce UHTC-based ceramics, which has the potential to create parts of complex geometries devoid of joints.

© Copyright 2020 by Shashvat Tejaskumar Mehta

All Rights Reserved

Additive Manufacturing of Ultra-High Temperature Ceramic (UHTC) Composites
using Electron Beam Melting Process.

by
Shashvat Tejaskumar Mehta

A Thesis submitted to the Graduate Faculty of
North Carolina State University
in partial fulfillment of the
requirements for the degree of
Master of Science

Mechanical Engineering

Raleigh, North Carolina
2020

APPROVED BY:

Dr. Chengying Xu
Committee Chair

Dr. Timothy Horn

Dr. Afsaneh Rabiei

Dr. Manoj K. Kolel-Veetil

DEDICATION

To my parents and my sister, whose support has been a constant source of motivation throughout the duration of this research.

BIOGRAPHY

Shashvat was born and raised in Ahmedabad, India. After graduating from high school in 2014, he joined the Nirma University in Gujarat, India, to pursue B.Tech. in Mechanical Engineering. Upon receiving his bachelor's degree in 2018, he decided to pursue a Master of Science in Mechanical Engineering from North Carolina State University. His work focuses on testing the feasibility of manufacturing UHTC composites using the Electron Beam Melting process.

ACKNOWLEDGMENTS

I would like to thank Dr. Cheryl Xu for her unwavering support and guidance for the duration of my graduate studies. Her constant belief in me has been a huge morale booster in times of uncertainty when things did not go as planned. I would also like to thank Dr. Tim Horn, for serving as my graduate advising committee member and always showing me the path forward. His passion for the field has been a source of inspiration and instilled the curiosity in me that led to pursuing this thesis. I would also like to thank Dr. Afsaneh Rabiei and Dr. Manoj Kumar Kolel Veetil for serving as my graduate advising committee.

I would also like to thank the entire team at the CAMAL Lab, ISE, NCSU for helping me with the experiments, and Dr. Xu's research group for their guidance. I would also like to thank my friends who were a constant companion on the coffee breaks; their company was far more rejuvenating than the espresso itself.

Finally, I would like to thank my parents Aradhana and Tejas, and my sister Ashaka, for always being there for me, and this would not have been possible without their encouragement and support.

TABLE OF CONTENTS

LIST OF TABLES	vii
LIST OF FIGURES	viii
Chapter 1: Introduction	1
Chapter 2: Literature Review	7
Additive Manufacturing	7
Electron beam Melting.....	12
Mathematical modeling for Electron Beam Melting	22
Feasibility of ZrB ₂ – SiC mixture UHTC manufacturing using EB-PBF.....	25
Feasibility of ZrB ₂ – ZrSi ₂ mixture UHTC manufacturing using EB-PBF	28
Chapter 3: Material Preparation and Experimentation	35
Powder characterization.....	35
Powder Particle Morphology	35
Powder Density.....	37
Powder Size Distribution	38
UHTC Sample preparation for EB-PBF Process	41
Experimentation	43
Chapter 4: Mathematical modeling of Electron Beam Melting for UHTC	48
FEM models for EB-PBF process	49
Material properties for ZrB ₂ – 30 vol% ZrSi ₂	52
Effect of porosity on the thermal properties	58
Modeling the heat source for Electron Beam Melting.....	61

Chapter 5: Results and Discussion	63
Simulation Results	63
Experimentation results	68
Processed track observation	69
Comparison of Simulation and Experimental results	81
Chapter 6: Conclusion	85
References	87
Appendices	97
Appendix 1 - Table of electrical resistivities of all the ceramics considered as additive	98
Appendix 2 – HAZ Dimensions observed from the FEA model simulation and experimentation	100

LIST OF TABLES

Table 2.1	Properties of ZrB_2 and $ZrSi_2$	29
Table 2.2	Electrical conductivities of ZrB_2 mixed with SiC, $MoSi_2$, and $ZrSi_2$	30
Table 2.3	Material properties of Titanium as gathered from ASM Matweb website.....	31
Table 2.4	Properties of different combinations of ZrB_2 and $ZrSi_2$	32
Table 3.1	Results of the Pycnometer density measurement	38
Table 3.2	Results of the MicroTrac Laser Diffraction	41
Table 3.3	Process parameters for the planned melt tracks on the pucks as per figure 3.11	44
Table 4.1	Temperature dependent properties of $ZrB_2 - 30$ vol% $ZrSi_2$	57
Table 5.1	Constant process parameters for simulating the mathematical model	65
Table 5.2	EDS Analysis of all the tracks.....	80

LIST OF FIGURES

Figure 1.1	Structure of a UHTC Leading edge in a Hypersonic vehicle	2
Figure 1.2	Porous material or slots of fixed size are used, and plenum chambers of various sizes distribute the coolant	2
Figure 2.1	Example of topology optimization applied to a component for a space flight.....	10
Figure 2.2	Schematic of Arcam AB EB-PBF machines	17
Figure 2.3	The phases of the EB-PBF process.	20
Figure 2.4	Schematic diagrams of the standard melt strategy employed in the EB-PBF machine.....	20
Figure 3.1	SEM imaging of ZrB_2 powder at 950x magnification	36
Figure 3.2	SEM imaging of $ZrSi_2$ powder at 1000x magnification.....	36
Figure 3.3	EDS analysis of the starting ZrB_2 powder.....	37
Figure 3.4	EDS analysis of the starting $ZrSi_2$ powder.....	37
Figure 3.5	Laser diffraction powder measurement based on the Fraunhofer diffraction principle.....	39
Figure 3.6	Numerical size distribution of the UHTC powder combination experimented.....	40
Figure 3.7	Volumetric size distribution of the UHTC powder combination experimented	40
Figure 3.8	Pucks pressed at 8 MPa for 5mins, ready to be heated	42
Figure 3.9	Pucks placed in the Stainless-Steel baseplate at CAMAL	42
Figure 3.10	Temperature profile for heating the pucks in the furnace	42
Figure 3.11	Layout of the 1D tracks planned for $ZrB_2 - 30 \text{ vol\% } ZrSi_2$ pucks placed on the stainless-steel baseplate placed in the EB-PBF machine.....	43
Figure 3.12	Inside view of Arcam S12 set up for the experiment	46

Figure 3.13 Thermal camera and backscatter electron detector attached to the top of the Arcam S12.....	46
Figure 4.1 Comparing the results of Zimmermann and Touloukian for thermal expansion strain.....	54
Figure 4.2 Comparing the results of Zimmermann and Touloukian for density	54
Figure 4.3 Variation of the specific heat capacity with temperature based on NIST-JANAF tables	55
Figure 4.4 Variation of thermal diffusivity based on the work by McClane	55
Figure 4.5 Comparing the thermal conductivities of bulk ZrB ₂ , ZrSi ₂ , and the proposed combination of ZrB ₂ – 30 vol% ZrSi ₂	56
Figure 4.6 Temperature-dependent thermal conductivity of the powder bed.....	60
Figure 5.1 Solid model adopted for the transient thermal FE analysis.....	63
Figure 5.2 Schematic of molten pool width as measured from simulation results.....	64
Figure 5.3 Schematic of molten pool depth as measured from simulation results	64
Figure 5.4 Variation of the HAZ dimension with changing process parameters	67
Figure 5.5 Temperature dependent thermal conductivity of Ti64 (based on the work of Neira Arce) and ZSZ, where ZSZ is ZrB ₂ – 30 vol% ZrSi ₂	68
Figure 5.6 Variation of surface roughness and melt consolidation with changing process parameters.....	69
Figure 5.7 Laser microscope images for the mentioned process parameters	70
Figure 5.8 Optical imaging of the HAZ tracks on the pucks for 5x, 10x, and 20x magnification	72

Figure 5.9 Partially and unmelted ZrB_2 particles can be seen engulfed in the melted and solidified $ZrSi_2$	73
Figure 5.10 Surface texture of the track with the process parameter of 500 W beam power and 750 mm/s scanning speed with Laser Confocal Microscope	74
Figure 5.11 Surface texture of the track with the process parameter of 500 W beam power and 1000 mm/s scanning speed with Laser Confocal Microscope	74
Figure 5.12 SEM image of process parameter 1000 W beam power and 1000 mm/s scanning speed.....	75
Figure 5.13 SEM image of the process track for sample P2 – Run 4 for electron beam power of 1000 W and scanning speed of 1000 mm/s	78
Figure 5.14 Comparison of the top surface texture for metal and UHTC	79
Figure 5.15 Proposed processing window based on the experimental results for manufacturing ZrB_2 – 30 vol% $ZrSi_2$ using the EB-PBF process	81
Figure 5.16 Heat-affected Zone of ZrB_2 – 30 vol% $ZrSi_2$ melted by an electron beam with varying scanning speed and line energy	82
Figure 5.17 Comparison of simulation and experimental results for beam power 500 W	83
Figure 5.18 Comparison of simulation and experimental results for beam power 1000 W	83
Figure 5.19 Comparison of simulation and experimental results for beam power 1500 W	84
Figure 5.20 Comparison of simulation and experimental results for beam power 2000 W	84

CHAPTER 1

INTRODUCTION

Environments of thermal extreme lead to the degradation of a material because of enhanced oxidation in the atmosphere and reduced mechanical properties at elevated temperatures. This scenario arises during the re-entry of space vehicles and during the flight of hypersonic aircraft. Improved materials are needed to withstand the conditions encountered by wing leading edges and propulsion system components in hypersonic aerospace vehicles as well as the extreme conditions associated with rocket propulsion. The combination of extreme temperature, chemically aggressive environments, and rapid heating/cooling is beyond the capabilities of current engineering ceramics [1]. The ceramics being used currently to tackle thermal extremes in a laboratory or industrial environment are not suitable candidates for use in the above-mentioned applications. To tackle the same, Ultra-high Temperature Ceramics (UHTC) are being developed specifically for this application.

Ultra-high temperature ceramics are not clearly defined in the literature. The most common traits of UHTCs are the high melting point. A material that melts at a temperature above 3000 °C can be defined as a UHTC [1]. Another method to define UHTCs is the highest operating temperature in air. The temperature of 2000 °C has been cited as a cut-off for a material to be categorized as a UHTC [1]. The most common definition is a chemical one, stating that the borides, nitrides, and carbides of early transition metals possess the required properties of UHTCs. The research for UHTCs was spearheaded by NASA (and its predecessor agency NACA) [2]. Bell X-1, the first flight to fly faster than the speed of sound, was being explored by the agency when it concentrated research on the search for better materials to withstand the thermal temperature extremes. Ames

and Man research labs of the agency conducted experiments on UHTCs in the 1960s and 70s but were later not pursued. The work was revived by the Ames research lab to explore the materials for sharp leading edges. UHTCs are best suited for specialized Thermal Protection System (TPS) applications for which other material systems are not as capable or straightforward or their capabilities are required when active cooling is not feasible. [3].

To reduce aerodynamic drag and increase lifting force and maneuverability, hypersonic flight vehicles have leading edges with radius as low as 15 mm [4]. As a result, the leading edges are subjected to extreme heat flux at the stagnation point ($>20 \text{ MW m}^{-2}$); correspondingly, the temperature of the surface can exceed the exploitation temperature of current materials. Currently, UHTCs are manufactured in parts using Hot Isostatic Pressing (HIP), Pressure-less sintering (PLS), and Spark Plasma Sintering (SPS) and are joined together to produce the final shape, as shown in figure 1.1 [3]. The leading edge is manufactured in parts owing to the process capabilities of PLS, HIP, SPS, etc. Additive Manufacturing (AM) can facilitate the entire leading edge to be made of a single part without joints including curvatures, with the only restriction being the machine tool working dimensions. NASA has been working on researching convective film

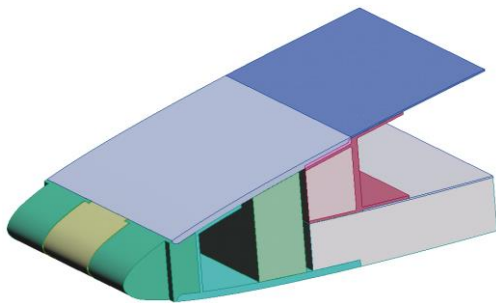


Figure 1.1 Structure of a UHTC Leading edge in a Hypersonic vehicle [3].

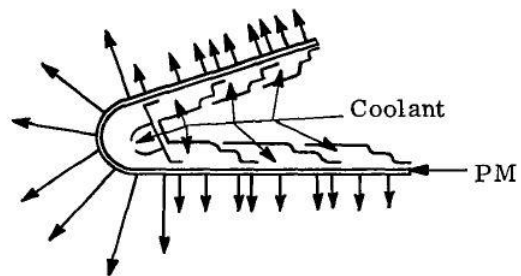


Figure 1.2 Porous material or slots of fixed size are used, and plenum chambers of various sizes distribute the coolant [5].

cooling on Hypersonic Mach 6 vehicles [5], [6]. The convective film cooling requires small channels as fluid passages and heat exchangers to transfer the thermal energy, built in the wing system. HIP, PLS, and SPS do not allow manufacturing pressed parts with internal channels and cavities due to the nature of these processes. These processes are limited to manufacturing parts that are axial and/or symmetric, mostly consisting of basic shapes. AM processes facilitate the manufacturing of parts of the required design. As seen in figure 1.2, an active cooling system can be integrated with UHTC Leading edges and the plenum chambers can be manufactured using the Additive Manufacturing process.

Transition metal oxides, borides, carbides, and nitrides have been researched as potential UHTCs for use in the environment of extreme thermal and material loadings. The relatively good oxidation resistance of refractory diboride compounds, compared to other refractory intermetallic compounds has focused many research efforts into detailed investigations of transition metal diborides of group IV and V [7]. Based on their melting point and the chemical properties, borides were opted as better alternatives. Borides of Zirconium and Hafnium proved to be two most suitable ceramic that would serve the purpose of UHTCs owing to their oxidation rates for high-temperature applications. Literature study has found them to be promising candidates based on their melting temperature and thermochemical stability [1]. Exhaustive research has been conducted on the properties of both ZrB_2 and HfB_2 [8] and both the ceramics possess desirable mechanical and chemical properties. Additives have been added and analyzed to study their behavior during sintering and in operation. Additives have been known to lower the sintering temperature of the borides and impart flexural strength to the UHTC composite. SiC has been promoted by many researchers, along with NASA Ames research center [3], as an additive in

manufacturing UHTC with HfB_2 and ZrB_2 [1]. Research has revealed that 20% SiC is the optimal condition for mixing with HfB_2 and ZrB_2 to impart flexural strength, toughness and increased mechanical properties.

Additive Manufacturing (AM) processes are layered manufacturing processes that create entire parts by dividing them into layers and consolidating material at each layer. Thermoplastics have been researched extensively for AM and machines ranging from desktop-size to industrial-scale are available in the market. On the other hand, metal additive manufacturing processes are currently in the research stage spearheaded by universities and national labs across the country. The ability to create parts with intricate details and internal cavities of superalloys and expensive space research materials justify the initial investment. Amongst all the Metal AM processes, Powder Bed Fusion (PBF) facilitate more complex geometries to be manufactured as compared to the Directed Energy Deposition and Binder Jetting processes that have higher number of publications. The feedstock is in powder form for PBF processes which are easier to produce for superalloys, as compared to sheets and blocks for starting material. The energy source is either a laser beam or an electron beam, enabling directed energy transfer across the powder bed and imparting flexibility in the part design. No binders are required unlike the Binder Jetting process and it is easier to create a support structure for the part in the powder bed. Out of the two energy sources, for this research Electron Beam provided better processing conditions like the presence of vacuum and better beam control, and hence Electron Beam Melting (EB-PBF) process was researched as a manufacturing option for the UHTCs. The presence of a vacuum, the ease of deflection of the electron beam as compared to the laser, controlled cooling of the part, material

sensitivity, and the power intensity make electron beam melting a more suitable option for manufacturing UHTCs.

Out of HfB_2 and ZrB_2 , Hafnium based compounds might be instable on interacting with the electron beam and react explosively. For this research, ZrB_2 will be analyzed for its feasibility to be manufactured using the Electron Beam process. Successfully manufacturing UHTCs of intricate shapes with internal cavities will open a whole new area of research and application. The restriction on the UHTC shapes due to the current process capabilities is imposing a limit on the complete exploitation of the advantages of the material properties of such materials.

ZrB_2 has a melting point of $3250\text{ }^\circ\text{C}$ and can sustain elevated temperatures above $2000\text{ }^\circ\text{C}$ in the air without significant oxidation to degrade its surface quality making it an ideal candidate to serve as a UHTC and is justified by the extensive research carried out on it by the ceramic community [1]. However, this higher melting point makes it difficult to process it using the Electron Beam technique. For this reason, it was mixed with an additive that facilitated the melting and solidification process of the powder in the EB-PBF machine. Various properties were considered for the same, including the melting point, electrical conductivity, thermal properties, and oxidation resistance of the additive.

The search for the new material was to fulfill the following initial requirements:

- The new material should melt in the available beam energy density.
- The electrical conductivity of the powder should promote sufficient beam coupling and charge-energy transfer to consolidate the powder material.

After researching various materials, $ZrSi_2$ was opted for experimentation in this process. It satisfied all the requirements for the process. The mixing proportion was determined based on electrical conductivity. 30% volume ratio of $ZrSi_2$ has the highest conductivity for sintered parts. In the EB-PBF process, a pre-sintering step is included to sinter the powder bed lightly to create a pathway to ground the circuit and as a mechanical resistance to electrostatic charging. This ensured that the electrical properties of the sintered part can be applied to the powder bed following the pre-sintering step and the neck formation ensured electrical conduction in the powder bed for circuit completion.

In this research, experiments were performed with the Finite Element Analysis (FEA) simulation results to assess the feasibility of the EB-PBF process for UHTC. The experimental results were compared with the simulated results and were found to be in proximity, and hence validating the FEA model. Process parameters for manufacturing $ZrB_2 - 30 \text{ vol}\% ZrSi_2$ have been presented.

CHAPTER 2

LITERATURE REVIEW

2.1 Additive Manufacturing

Additive manufacturing (AM) is an emerging concept of bottom-up approach for layered manufacturing. This class of processes consist of creating parts layer-by-layer to generate the final part. ASTM F42 Committee on AM defines it as ‘process of joining materials to make objects from 3D model data, usually layer upon layer, as opposed to subtractive manufacturing methodologies’ [9]. With the advent of additive manufacturing, the use of polymers to create prototypes has increased drastically. Soon, the additive manufacturing of metals began and processes like binder jetting, material jetting, powder bed fusion, direct metal deposition, etc. evolved which enabled the additive manufacturing of from metal powders. Initially, the additive manufacturing processes were primarily used for prototyping and tooling purposes, but continuous research has promoted this class of processes to be used in direct manufacturing [10]. This breakthrough benefitted the aerospace, nuclear, and the biomedical industry the most. Not ideally the best process for mass production, metal additive manufacturing facilitates producing parts with intricate details and internal cavities as a single part, which traditionally was carried out by fabricating the product in separate components and joining the same through welding and other traditional processes. Engine nozzles, turbine blades, etc. are some of the critical parts that are manufactured using metal additive processes. Building on the success of Metal Additive manufacturing, the idea of exploring the option of manufacturing Ultra-High Temperature Ceramics (UHTC) using additive manufacturing was researched in this thesis.

Additive manufacturing is one of the forerunners in disruptive manufacturing, providing designers with extended freedom and reduced limitations in realizing their innovative designs and facilitating manufacturers to produce parts with intricate design and complex geometries. Institutions like ASTM and ISO have developed codes and standards to define and classify the existing additive manufacturing technologies available, with an effort to universalize this disruption. Additive manufacturing has the potential to radically change how products are made and distributed [11]. Implementation of AM technologies effectively removes the need for tooling in production, reducing production time, and automates the process with minimal human interaction restricted to the initial setup of the machine tool and removal of the finished product. 3D printing produces near dense products with similar densities as of wrought and cast products [11]. AM promotes innovation in the product design, with a reduction in the cost of the part manufactured. AM is best suited to produce small-sized batches with frequent variations in the product design, aiding in the prototyping, and testing of the new product. However, mass production of parts built using AM is not yet adopted by industries worldwide as the initial costs are heavy. A Delphi study states that more than 50% of additive manufacturing capacity will be in-house by 2030 [12]. According to Busachi [13], 74% of the total cost of setting up an additive manufacturing machine is the cost of the machine tool. Compared to it, the costs of running the machine, energy requirements, raw materials, and finishing operations are lower. AM can have a tremendous impact on the defense sector. In another study by the same author, the results show that AM is an enabler of Just-In-Time and delocalized manufacturing which combined with design freedom and fully dense metal production can have a major impact on the support services sector [14].

Additive manufacturing has numerous advantages over the traditional processes. Some of the AM processes take place in a vacuum which prevents oxidation on the part. The expiration of patents in the past decade has resulted in an explosion in the numbers of AM technologies being developed and has been made available to manufacturers and designers alike. This disruption has helped in the reduction in the time-to-market time of the product and enhanced customization [15]. Especially, the technologies for producing parts with thermoplastics have become cheap and can be found in almost all academic institutions and small-scale industries. These technologies convert Computer-Aided-Design (CAD) data in a file format compatible with the machine tool, and different machine tool manufacturers might maintain a restriction on the file type for their machine tool. STL files have curbed this issue to a large extent, but still require further enhancements to reduce the errors. Any inherent errors in the CAD geometry will lead to the part being produced with the same errors. AM machine tools can be programmed to build a unique part, and this removes the cost of tooling and setup that is involved with traditional manufacturing. This results in a reduction in the lead time as tools are not required to be produced and instigating flexibility in the supply chain. This facilitates customizable production as opposed to mass production and is ideal for applications that require unique design and of lower counts, as in aerospace, medical, and automobile industry. Additive manufacturing processes require lesser energy, no cutting fluids or coolants and the absence of tool wear out reduces the carbon footprint [12]. Structural optimization ideas can be conceptualized using AM. The optimization algorithms in CAD/CAE software result in geometries that are difficult to produce through traditional manufacturing, starting from stock and removing a significant amount of material to reach the final shape. This is expensive and in the majority of the cases, the cost of manufacturing such a geometry outweighs the benefit associated with optimized geometry. AM technology helps achieve this to a large extent and an

example of the same is shown in figure 3. With the parts being produced layer-by-layer, it has become possible to manufacture geometries produced by the optimization software without significant editing, with figure 2.1 being an example of the same [16]. The part can be produced without any joints and with minimal post-processing operations which is not possible with traditional approaches. Inclusion of joints is a point of stress concentration and is usually accompanied by the residual stresses in the part. Manufacturing without joints is one of the major advantages of AM.

Most of the additive manufacturing technologies are layer-based processes that induce a strain-step error in the produced part [11]. The minimum wall thickness in the additive manufacturing processes is dependent on the powder layer thickness and the processing method[17]. Currently, only a few metal composites are being produced using additive manufacturing technologies, and exhaustive research and experimentation are required to measure the feasibility of novel materials [15] which is the issue addressed in this thesis. The size of the part being manufactured is limited by the size of the machine tool used for production. A part bigger than the machine tool requires



Figure 2.1 Example of topology optimization applied to a component for a space flight

(a) Camera star bracket geometry selected for optimization and 3D printing

(b) Renderings of topology optimized camera star tracker bracket [16].

joining, which was one of the reasons for adopting additive manufacturing for critical parts. The parts made as a result of AM need post-processing depending on the process and material issued. Thermoplastic parts need to be washed and cleaned in a chemical solution based on the process. Metal parts have a rough surface and require finishing operation to generate the final desired geometry. The initial cost of establishing an AM center is high, with the Fused Deposition Modeling machines available within a thousand dollars to high-end EB-PBF machines costing half a million dollars. But once the machine has been set up, it can be used to manufacture several parts and critical applications can leverage the cost-benefit ratio to the positive side. Additive manufacturing processes have the capability to manufacture complex parts that have their properties comparable with the cast parts [18], [19].

The advantages of using AM surpasses the disadvantages and this led to the idea of opting for AM process to manufacture Ultra-High Temperature Ceramic. Significant research has not been done in manufacturing UHTC using AM. Considering the research being done for metal additive manufacturing, it was prudent to apply the same methodologies to ceramics. With the requirement for being able to manufacture UHTCs of complex shapes and geometry, the time to dive into this research has never been better. NASA has been testing AM in zero gravity in hopes of establishing on-demand manufacturing for astronauts. This would allow parts for maintenance and repair of the international space station to be manufactured in space [20]. Several institutions have modified existing AM machines to make it feasible to manufacture ceramics. Tweaking the industrial machines and producing AM parts might not be the best way to promote this technology as this results in a set of parameters that would not be available to every researcher. Hence, the research in this project will be done on industrially available machines and the process parameters will be

developed for the same. The results would be published making it easier for the entire research community and industry alike to extend this research and not devote time to fabricating a unique machine.

Additive manufacturing processes are not suited for large volume productions. The setup time required for producing one single run is high and is expensive if the application of the part is trivial. Manufacturing using AM is justified only for parts that are intricate in design, with internal chambers or cavities, and is expensive to produce in a limited quantity using the conventional manufacturing processes. AM would best dominate the low production-manufacturing sector for its customizability, short lead-time, and complex geometric capability [21]. Traditionally, the manufacturing industry has been prevalent in manufacturing high volume goods with a low amount of design changes. Principles of Design for Assembly and Design for Manufacturing have succeeded in creating a set of universal guidelines that most designers adhere to and making it difficult to change the fundamental design of the product as that results in expensive changes to the existing production line. A small object, like a plastic bottle cap, is best suited for manufacturing using injection molding that creates parts with a rate that is impossible with additive manufacturing in the present and near future.

2.1.1 Electron Beam Melting

Electron Beam - Powder Bed Fusion (EB-PBF) or Electron Beam Melting (EBM) is an additive manufacturing process that falls in the Powder Bed Fusion (PBF) class along with Laser Powder Bed Fusion (LPBF) being a companion of the process. PBF processes facilitate the manufacturing of near-net structures from raw powder and work on the bottom-up approach. This allows for

producing internal cavities and channels, which were difficult to produce using traditional manufacturing processes [22]. Both processes work on the basic principle of melting the powder in the powder bed using a high-intensity energy source, either electron beam or laser, followed by lowering the powder bed to repeat the process to form a new layer. LPBF has been investigated in depth over the last couple of decades and numerous materials have been manufactured using it. However, EB-PBF is only used for a few materials on the industrial level, and the search for compatible new materials is ongoing. The electron beam is easier to deflect using electromagnetic fields, enabling to achieve fast transition speeds as compared to mechanical elements in LPBF processes [23]. EB-PBF facilitates the development of planned heating and melting strategies to target selective melting of tracks on the powder bed, which is difficult with LPBF [22], [23]. EB-PBF requires a vacuum to function, which is a drawback as this requires additional equipment and setup. However, the presence of vacuum makes the oxidation less favorable as compared to an inert gas shielding of the material at high temperature and this is a huge advantage of EB-PBF for manufacturing materials with high affinity towards oxidation at elevated temperatures [11], [22], [23].

The loose powder, when first spread across the build platform is susceptible to picking up charge from interaction with the electron beam, a phenomenon in which the powder particles spread in the vacuum chamber, interfering with the electron beam and is not preferred, as this results in a part with defect, damages the electron beam column and the machine needs to be thoroughly cleaned before further production runs [22], [23]. Powder size distribution, density, and interparticle cohesive forces aid in predicting the occurrence of charging during the pre-sintering process.

EB-PBF process is used for manufacturing in sectors like aerospace and biomedical engineering. The main optimization target for aerospace designs is the reduction of weight. The parts are readily available for installation and testing and remove the long manufacture times for complex parts to be made ready for testing [22]. Metal alloys being used in aerospace applications are expensive and manufacturing optimized geometrical shapes from stock material increases the overall cost of the part. Boeing and Airbus are already using additively manufactured parts in both military and commercial airplanes [20]. The acceptance standards of EB-PBF proposals have also been published [24]. EB-PBF and LPBF facilitate weight reduction topology optimization techniques as it is easier to produce the part and grind the outer surface as compared to subtractive manufacturing that involves joints.

In metal additive processes, powder bed fusion processes have been known to produce parts with the most accurate details and strength, and so for manufacturing ceramics, powder bed fusion processes were chosen. Ultra-high temperature ceramics are used in environments of thermal extremes to shield the contained parts against the excessive heat generation. Electron Beam Melting process can manufacture near net shape parts with complex geometries and internal cavities. LPBF process takes place in an inert gas flowing atmosphere and this is critical as no impurity formation is desirable in UHTCs due to its application in mission-critical situations. In the electron-beam melting process, the entire process takes place in a vacuum around 10^{-3} Pa [25] providing a better option to resist oxidation as compared to an inert gas atmosphere. The rapid heating-cooling of the melted layer in LPBF and the conduction through the solid substrate resulted in temperature variations in the part. Thus, thermal stresses are produced, and the material needs to be ductile enough to sustain these stresses, or else it might result in the delamination of layers.

In EB-PBF, the parts are cooled in a vacuum with radiation in the chamber and conduction to the base being the heat transfer mechanisms. Thus, EB-PBF was selected for manufacturing UHTCs for this research project.

The EB-PBF process behaves similarly to a welding machine and the operating principle is similar to an electron microscope [25]. In the EB-PBF process, an electron beam with high energy density impinges on a powder bed. The energy transfer takes place between the electrons and the powder particles and the electrons travel till they reach their threshold energy. The energy transfer is high enough in the Heat Affected Zone (HAZ) to result in temperature above the melting point of the powder material resulting in a local melt pool being generated. Following that, the powder bed is lowered by one layer-thickness, fresh powder is spread on the melted layer and another cycle follows. The layers are pre-sintered by bombarding a defocused electron beam on the cross-sectional area to initiate necking among the powder particles to avoid smoke. The built part is cooled to the atmospheric temperature in the vacuum environment. Figure 1, a schematic of the EB-PBF machine with the electron gun and the chamber presents a better understanding of the setup of the Electron Beam Melting machines. In the EB-PBF process, the powder bed is initially processed with low-intensity electron beams to lightly sinter the powder particles. This process is sometimes referred to as “jump-safe” process and ensures that a higher powdered electron beam can jump from one place to another on the bed, and the next preheat strategy is the “melt-safe” process, which uses the beam of a higher power to consolidate the powder particles further and prevent smoke during the melting process, which uses an electron beam of high intensity with a smaller spot size to melt the powder [26].

The experiments were carried out in the Center for Advanced Manufacturing and Logistics (CAMAL) Lab at NCSU. The lab has three EB-PBF setups, Arcam S12, A2, and Q10 with the experiments performed on the S12 machine. Arcam AB is one of the leading manufacturers of the EB-PBF machines and they have developed a set of metal powders that work the best on their machines and are industrial alloys. It includes the Ti6Al4V alloys, CoCr and Nickel 718. Research has also been done in manufacturing Stainless Steel, Tool Steel, Copper, etc. on EB-PBF machines [22]. For the powder to be manufactured using EB-PBF, it should be electrically conductive. The thermal properties should be such that the heat is confined to a small region, not spread out to a large extent which would result in not achieving the melting temperature due to an excessively high thermal conductivity for the supplied energy density, and should not be low enough to cause the evaporation of the metal powder itself which can occur as a combination of low thermal conductivity.

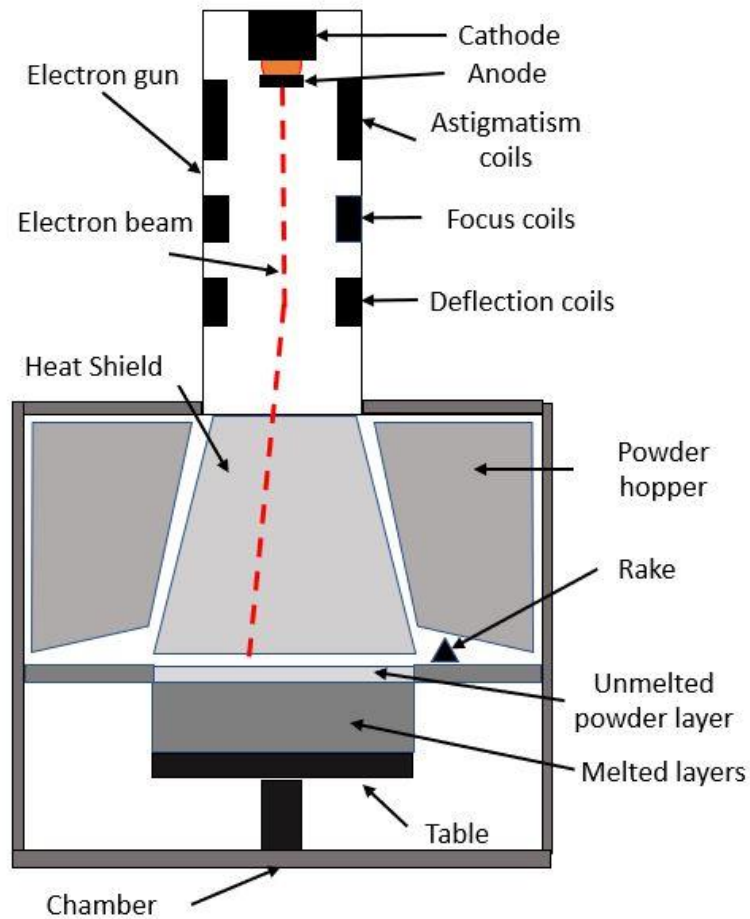


Figure 2.2 Schematic of Arcam AB EB-PBF machines.

The machine tool specifications of Arcam AB S12 EB-PBF machine are as follows:

- Building tank volume 250 x 250 x 200 mm (W x D x H)
- Maximum build size 200 x 200 x 180 mm
- Accuracy ± 0.4 mm
- Melting speed Up to 60 cm³/h (material-dependent)
- Layer thickness 0.05–0.2 mm (material-dependent)
- EB scan speed > 1000 m/s
- EB positioning accuracy ± 0.05 mm
- Beam power 3500 W

- Power supply 3 x 400 V, 32 A, 7kW
- Size and weight 1850 x 900 x 2200 mm (W x D x H) 1420 kg
- Process computer PC, XP Professional
- CAD interface Standard: STL
- Network Ethernet 10/100
- Certification CE

The build chamber contains mechanical parts like the build tank, rake, the hopper and feeder system for the powder. The build tank is a steel tank with allowable movement in the direction of build. The parts are usually built on a start plate that is heated before initiating the part building. The powder is fed into the hopper from where the rake distributes a calibrated amount of powder onto the powder bed. The powder layer thickness is set in the machine tool depending on the material being melted. The electron gun is operated at a vacuum level of 10^{-7} and 10^{-6} bar and the chamber is held between 10^{-4} and 10^{-3} bar [27]. The electron beam consists of a cathode and an anode. Astigmatism, focus, and deflection coils are provided for better control over the path traversed by the beam. The tungsten electrode emits electrons due to the potential difference between itself and the anode. The electrons which are not absorbed by the anode eventually interact with the part. The cross-sectional geometry of the beam is controlled by the focus coils and the astigmatism coils. The position of the beam over the surface of the part in the build plane is controlled by a set of deflection coils [27]. Proper calibration needs to be done to ensure the rake system is depositing the correct amount of powder. A shortage of powder can cause re-melting of the previous layers, whereas an excess of the powder results in uneven melting, delamination and can also cause smoke. The electron beam also needs to be calibrated for its accuracy in position

by calibrating the deflection coil magnetic fields and focusing of the beam onto the part by calibrating the focus and astigmatism controls.

The working of an EB-PBF machine starts with the preheating of the build plate to a suitable temperature. The first step of the cycle is preheating and sintering. This also results in the necking of the powder particles and provides electrical circuit completion [27]. Parts with overhangs require support and sintering with higher intensity can result in creation of supports with considerable strength. Then the main step of melting is carried out wherein a highly focused electron beam traverses over the part cross-section to melt the geometry. Each of these steps consists of an outer contour defined by the perimeter and the inner space is filled by the raster used to melt the inner bulk of the part. Figure 2.3 provides a better understanding of the EB-PBF process [25]. Figure 2.4 describes the different melt scan strategies that are commonly used in the melting stage [28]. Figure 2.4(a) is the default option in Arcam machines with a feature to select up to five contours and fill the inner region with hatches. Other types of contour and raster patterns researched by the researchers in the community are shown as Figure 2.4(b) to 2.4(e).

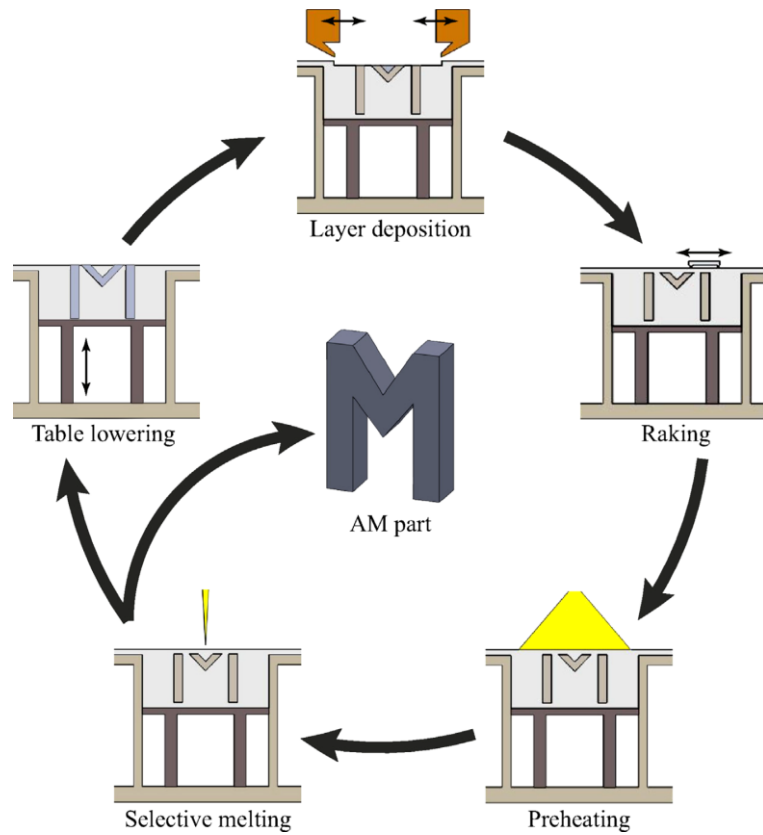


Figure 2.3 The phases of the EB-PBF process. [25]

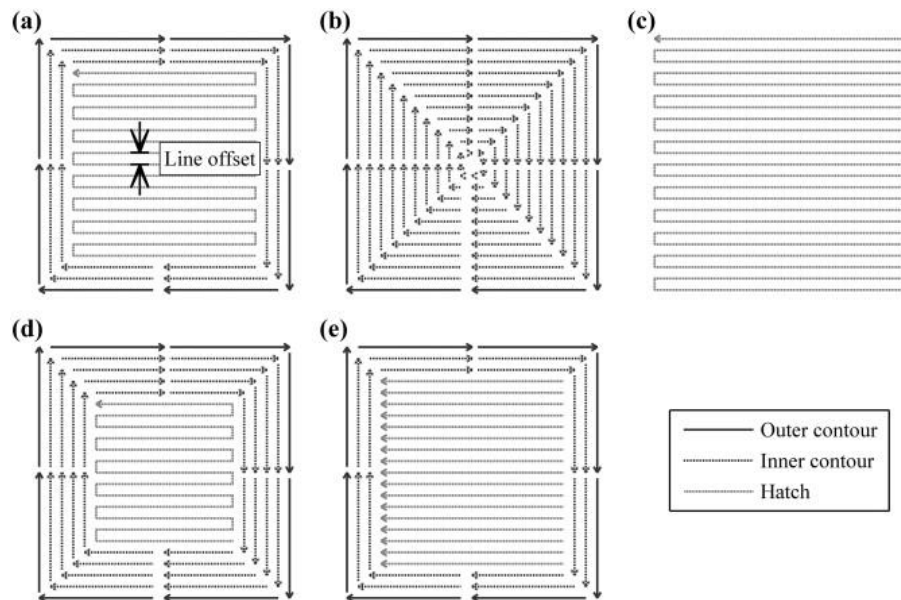


Figure 2.4 Schematic diagrams of the standard melt strategy employed in the EB-PBF

machine (a). Other strategies used various researcher (b)-(e). [25]

Arcam has developed a select few metal alloys that are best suited for processing under the electron beam. The metal alloy powders are highly conductive and have proven manufacturability. ZrB_2 has a high melting point and it is difficult to melt it with the current capabilities of the Arcam electron gun. The melting point of ZrB_2 is around 3000 °C, and melting this material is difficult in the EB-PBF. Additives that possess a melting point in the range of the Arcam developed alloys can be added to lower the melting point of the entire mixture. For this task, various ceramics were studied. The idea is to melt a secondary material that will melt, wetting the ZrB_2 powder particles and solidification will serve as a joint between the UHTC powder particles.

Modifying the EB-PBF machine to suit the material into consideration by changing the operating parameters and altering the original design, making the stability and control system of the machine tool at risk, is difficult. In this situation, the application of the modeling and simulation of the additive manufacturing process using an iterative method makes it easier to assess the feasibility of new material and evaluate the process parameters for the same.

EB-PBF is a preferred process to manufacture ZrB_2 based ceramic composites as the material is susceptible to contamination and the inclusion of impurities formed on reacting with oxygen, hydrogen, and nitrogen results in undesirable phases that reduce the overall property of the part manufactured. The oxides of Zirconium and Boride are brittle with reduced mechanical properties and fracture toughness. Hence, avoiding the formation of such compounds is a critical step for manufacturing ZrB_2 to be used in environments of thermal extremes. The mechanical and electrical properties of the additively manufactured parts are different from the traditionally manufactured

parts and hence proper testing and validation are required before their application in the aerospace industry.

2.1.2 Mathematical modeling for Electron Beam Melting

Mathematical modeling of the electron beam process aids in determining the process parameters for experimentation. Many researchers have developed the process parameters by experimenting with different combinations and trying out a trial-and-error approach. This leads to increased experimentation timings, a higher amount of resources being invested, and a greater number of samples to analyze. This approach has resulted in accurate and optimized process parameter determination for a wide range of materials, but the availability of mathematical models would have expedited the process and saved the invaluable time of the researchers. Although control of solidification texture can be achieved by experimental trial and error optimizations, the number of experimental trials can be significantly reduced by using numerical models capable of describing the underlying physics [29].

Galati et al. [25] have presented a brief overview of different types of models developed for the EB-PBF process. More complex models take an increased amount of time to simulate the process, sometimes months [25]. These models involve a high level of complexity, like the grid-based discrete element approach [30], mesoscopic modeling with each powder particle modeled into the powder bed [31], [32], and the Hertz-Mindlin contact models [33]. These models had the lowest amount of approximations and hence resulted in an accurate representation of the process. However, these models were computationally expensive, required a large amount of time, and were not best suited to analyze a wide range of process parameters, especially for testing the

feasibility of new material. Instead, many researchers adopted the method of lower complex models representing the powder bed as a continuum with reduced properties to incorporate the effect of porosity on the thermal properties. Uncoupled thermal models as such were implemented by Qi, Yan, Lin and Zhang [34], Mahale [27], Neira Arce [35], Zäh and Lutzmann [36], Galati, Iuliano, Salmi, and Atzeni [37], Chou [38], and various others. The primary objective of these authors was not to understand the various phenomenon occurring at the microscopic level during the EB-PBF process, but rather to develop process parameters and conduct experiments with these results. The powder bed is treated as a solid block and the heat source is applied as a planar heat flux on the element or voxel, traversing linearly in the direction of electron beam travel. The temperature generated is monitored in the process and distribution of the temperature becomes the selection criteria for downsizing the results.

For modeling the powder bed as a continuum, the material properties are reduced for that of the powder from the bulk material, which are significantly different. A material stage change aspect is also included which changes the material property from powder material to bulk solid material on melting and solidification of the melt track. Thus, the thermal behavior of the material is modeled as a function of temperature and material state of the layer. The heat transfer mechanisms in the models are coded for conduction in the bulk layer and radiation on the top surface. For the powder phase, heat transfer due to conduction at the contact regions and radiation in between the particles is assumed. Various complex physical phenomena in the heat-affected zone are responsible for the heat transfer. The most widely cited approach is the lattice Boltzmann approach developed by the Körner group [32].

Mathematical models and experimental results developed so far are mostly for metallic alloys like Ti-6Al-4V, IN 718, etc. Jamshidina et al. [39] have presented the numerical model for Ti64 and its comparison with the experimental results. The most common approach to model the heat source is a Gaussian distribution [25], with the intensity decreasing in the direction of impingement. The electron beam has been modeled as a moving heat source that travels along the planned direction and jumping from one point to another on the surface. Other methods involved a uniform volumetric heat distribution that acted on successive voxels with increasing time step of the model [33]. Statistical methods have also been adopted to model the heat source, with the Monte Carlo model being one of them and most authors using the CASINO software [27], [37], [40].

For developing the mathematical model for EB-PBF processing of the UHTC materials, the powder packing density of the powder bed needs to be approximated. Numerous authors have approximated BCC packing of the powder bed, and some have assumed an arbitrary value of 50% for the model. This value of density was used in determining the thermal conductivity of the powder bed. The specific heat value of the powder bed was kept similar to the values of the bulk material, and the enthalpy of both the materials is fed into the mathematical model. The emissivity of the powder bed was also considered in the model. The consideration and computation of the same have been presented in the chapter on the mathematical model in the thesis. The model was analyzed for different combinations of the process parameters and the temperature profiles of each combination was studied. Based on the requirements of the EB-PBF process, the results were downsized to select a few which will be used in the experimentation phase. The developed mathematical model was compared with the results generated for Ti-6Al-4V due to it being the most widely used metallic alloy for additive manufacturing. Developing a working mathematical

model for EB-PBF processing of UHTC materials will ease the process of future research, by running the simulations before the experimentation, and saving time of the researchers. The model was developed using the continuum-based approach; however, the complexity can be increased to include the complex physical phenomenon that is ignored in this model.

Developing a new material for an existing manufacturing process is a lengthy process, intended to develop the process to improve the existing methods or test the feasibility of a new parameter. In this thesis, an attempt was made to manufacture UHTCs, a class of material, that has never been manufactured before using the Electron Beam Melting process. ZrB_2 was used as the test material due to its usage in a wide variety of applications. Experiments were performed in this research work and the mathematical model developed was the preliminary steps in determining the feasibility. The process parameters being developed are for Arcam AB EB-PBF machines, making it easier for the research community to contribute further instead of developing the same on a custom-built machine tool with parameters not possible on an industrial machine.

2.2 Feasibility of ZrB_2 – SiC mixture UHTC manufacturing using EB-PBF

ZrB_2 has been sintered for a single layer using electron beam with extremely high power settings on a custom set up, and the advantages over laser sintering have been researched [41]. However, ZrB_2 standalone cannot be manufactured using EB-PBF due to its high melting point. Additives were considered to lower the melting point and improve the sinterability. The addition of other ceramics has been proven to aid in this process. SiC is frequently used with ZrB_2 with conventional sintering. SiC fibers can be added to impart high thermal shock resistance and to avoid non-catastrophic failure. SiC has been added in powder, whiskers, and flakes form to the ZrB_2 matrix

to produce the final part. SiC when added to ZrB₂ aids in densification and also improve properties such as fracture toughness which is useful for its application for environments of thermal extremes. ZrB₂ containing ultrafine SiC powders (5, 10, 15, and 20 vol%) and no extra sintering aids, were mixed with SiC milling media, achieved full density for all compositions after HP at 1900°C with 30–40 MPa of applied pressure [42]. But it was found that the properties of SiC in the fiber form deteriorated above 1700 °C and ZrB₂ requires a sintering temperature above that. ZrB₂ with 20 vol% SiC is optimal for processing conditions based on densification, mechanical properties, and oxidation resistance [1].

The melting point and electrical conductivity of SiC was also carefully studied to determine the feasibility using the EB-PBF process. The melting point of the Titanium alloys provided by Arcam AB are in the range of 1600 – 1660 °C whereas the melting point of ZrB₂ is 3000 °C and the melting point of SiC is 2700 °C [43]. Simulations were carried out to calculate if this temperature was achievable using the maximum power limits available in the EB-PBF machines. The electrical conductivity of SiC is low and hence the resulting combinations are not fully compatible with the machine. The materials provided by Arcam have their electrical resistivity in the range of 0.52×10^{-4} ohm-cm to 1.78×10^{-4} ohm-cm. The electrical resistivity of SiC is in the range of 10^7 ohm-cm, which is significantly higher than the Arcam provided materials and difficult to manufacture using EB-PBF as it will not conduct electricity. The electrical conductivity of ZrB₂ is higher than that of Arcam Ti6Al4V powders and can conduct electricity well enough to form an electrical circuit to mitigate charging.

Since the two mentioned ceramics have wide usage and are preferred over other ceramics, a literature review was conducted to find any possible combinations or additions of other materials that might result in increasing the overall electrical conductivity of the mixture to enable it to conduct the electricity to raise its temperature. The addition of SiC to the surface Inconel 625 alloy has also been studied [44]. SiC wires have been manufactured using SiC slurry with Cobalt as a catalyst and processing using an electron beam, proving that the presence of a catalyst might aid in this process [45]. Another paper discussed the formation of SiC as an impurity when pure Si was used in EB-PBF. The SiC settled at the lower part of the layer and had to be machined. Research has also been done to add a layer of titanium on the SiC part using an intense electron beam[46]. Adding pure Si and C in the ZrB₂ powder might result in the formation of SiC in the final part, but it would also result in the formation of other components which would be undesirable. Another method researched was spraying Ti on SPS SiC part, and irradiating it with the electron beam, which resulted in a layer of SiC rich SiC-Ti composite on the top [46]. This gave way to manufacturing UHTC with spraying ZrB₂ on SPS SiC part and then processing it under EB-PBF. SiC composites with high electrical conductivity have been researched and manufactured but using these in our mixture would increase the cost greatly and it will be difficult to simulate and analyze. Since the electrical conductivity and melting temperature are a problem for the proposed project, it was decided to determine a range of electrical conductivity to determine the feasibility of the new materials.

Finding the electrical conductivity for all the materials that are provided by Arcam for EB-PBF, the range of their electrical conductivities was found to be 58.5×10^5 S/m to 596×10^5 S/m. The new proposed material can conduct electricity from the electron beam assuredly if its electrical

conductivity falls in this range, at least above the lower limit. The electrical conductivity of combined ZrB₂-SiC was found in a research paper [47]. The electrical conductivities were found as

- ZrB₂ – 10 vol% SiC: 15.3×10^6 S/m
- ZrB₂ – 20 vol% SiC: 11.6×10^6 S/m
- ZrB₂ – 30 vol% SiC: 8.86×10^6 S/m

The specimens were prepared by sintering, which can be assumed to be a similar representation of the pre-sintering process in an EB-PBF process. Another paper has presented the electrical conductivity of ZrB₂ – 20 vol% SiC as 9.76×10^6 S/m which was prepared by sintering under uniaxial loading [48]. This leads us to the conclusion that ZrB₂ – 20 vol% SiC is a potential candidate for manufacturing using the EB-PBF process. Also, SiC is found to damage the UHTC properties of ZrB₂ when used in the layered protection system [4]. SiC fibers can be added to impart high thermal shock resistance and to avoid non-catastrophic failure. However, the melting point of SiC is 2350 °C and this is more than the melting point of metals processed with EB-PBF. Along with SiC being an electrical insulator and decreasing the electrical conductivity of the overall mixture, the high melting point might prove to be a hindrance for processing with EB-PBF. Alternatives were searched for SiC to be mixed with ZrB₂.

2.3 Feasibility of ZrB₂ – ZrSi₂ mixture UHTC manufacturing using EB-PBF

Performing basic thermal calculations revealed that it would have been difficult to melt the ZrB₂ – SiC mixture with the available beam power and velocity capabilities. Further research was undertaken to find new ceramic material to replace SiC which had better electrical conductivity and lower melting point. A list of the possible material was prepared with electrical conductivity

and melting points, which is presented in appendix 1. Disilicides have been found to improve sinterability and prevent oxidation of the ceramic. They also impart high flexural-strength; and high thermal and electrical conductivity to the composite [49], [50]. Of these, the disilicides of transition metals are recommended as sintering aids [41], [51], [52]. Zirconium and Molybdenum disilicides have been reported as sintering aids used with ZrB₂ and both have given satisfactory results. From that list in appendix 1, two materials, MoSi₂ and ZrSi₂ were selected for further analysis as they satisfied the above requirements. It has been researched that the electrical conductivity of bulk MoSi₂ is 2.86×10^4 S/m and ZrSi₂ is 2.5×10^4 S/m which can aid in increasing the electrical conductivity of the mixture. Hafnium based alloys as additives also present excellent electrical conductivities, but they were not considered as their melting point is above 3000 °C. The effect of the addition of SiC, MoSi₂, and ZrSi₂ to ZrB₂ was also studied by Guo [49]. It was found that this paper is extremely insightful to the research as it presented an acute comparison of the materials being compared. ZrSi₂ has been found to reduce the process temperature to below 1700 °C and aids in achieving a relative density of nearly 99% when sintered. This temperature range is achievable in the EB-PBF machine and is relatively lower than the temperature required with MoSi₂. In this research, ZrSi₂ is used as an additive for ZrB₂ for the above-mentioned reasons, along with being an electrical conductor and having a melting point of 1650 °C. The properties of

Table 2.1 Properties of ZrB₂ and ZrSi₂.

Properties	ZrB₂	ZrSi₂
Melting point (°C)	3245	1620
Electrical conductivity (S/cm)	1.08×10^5	2.5×10^4
Thermal conductivity (W/m K)	60	97.2
Density (g/cm ³)	6.119	4.88
Powder size (microns)	40 - 100	45 - 75

both are presented in table 2.1. This melting point is at par with the melting point of Ti6Al4V which is provided by Arcam AB for producing EB-PBF parts on its machine tools. The electrical conductivity of ZrB₂ with SiC and ZrSi₂ has been determined by various researchers. The electrical conductivity of ZrSi₂ is 2.5×10^6 S/m [53]. Guo et al. [54] have provided an exhaustive list of the electrical conductivity of ZrB₂ mixed with MoSi₂, SiC, and ZrSi₂. Out of all the combinations tested, ZrB₂ - ZrSi₂ has the highest electrical conductivity. ZrB₂ mixed with ZrSi₂ vol% of 10, 20, 30, and 40 was found to have the electrical conductivity of 10.7×10^6 S/m, 11.6×10^6 S/m, 11.9×10^6 S/m and 9.6×10^6 S/m respectively. Out of these, 30 vol% of ZrSi₂ was selected as the additive

Table 2.2 Electrical conductivities of ZrB₂ mixed with SiC, MoSi₂, and ZrSi₂.

Composition (vol %)	Electrical conductivity (x 10⁴ S/cm)
ZrB ₂	4.5 – 10.3
ZrB ₂ - 30 SiC	4.2
ZrB ₂ - 10 MoSi ₂	8.11
ZrB ₂ - 20 MoSi ₂	7.22
ZrB ₂ - 40 MoSi ₂	7.48
ZrB ₂ - 40 MoSi ₂ – 5 SiC	7.35
ZrB ₂ - 40 MoSi ₂ – 10 SiC	6.04
ZrB ₂ - 40 MoSi ₂ – 20 SiC	4.07
ZrB ₂ – 10 ZrSi ₂	10.7
ZrB ₂ – 20 ZrSi ₂	11.6
ZrB ₂ – 30 ZrSi ₂	11.9
ZrB ₂ – 40 ZrSi ₂	9.6

amount for our experimentation. Various other properties were studied by Guo et al. for samples prepared by pressure-less sintering at 1650 °C in the Argon environment [54]. For this combination, the mechanical, thermal, and electrical properties were calculated for pressure-less sintering. These properties will be useful for simulations as they can be changed for porosity considerations and reduced density of the powder bed. In these papers, the authors have suggested that the highest electrical conductivity is for 30 vol% of ZrSi₂. For a higher concentration of ZrSi₂, the electrical conductivity decreases due to the increased resistance of ZrSi₂ and for lower concentrations, the electrical conductivity decreases due to the porosity effects. Initially, the physical, electrical, and thermal properties of the Titanium alloy Ti6Al4V were studied and compared with to determine the feasibility. Since this powder is provided by Arcam AB and has been proved to produce satisfactory parts, we shall compare the properties of this material with the proposed materials. From the ASM Matweb website [55], some of the important properties are shown in table 2.3.

Table 2.3 Material properties of TI6Al4V as gathered from ASM Matweb website. [55]

Property	Value
Density	4.43 g/cc
Ultimate Tensile Strength	950 MPa
Yield Tensile Strength	880 MPa
Poisson's ratio	0.342
Electrical Resistivity	178 μΩcm
Specific Heat Capacity	0.5263 J/g °C
Thermal Conductivity	6.7 W/m K
Melting point	1660 °C

Table 2.4 Properties of different combinations of ZrB₂ and ZrSi₂.

Density	g/cm³
ZSZ 1	5.97
ZSZ 2	5.85
ZSZ 3	5.73
ZSZ 4	5.61
Elastic Modulus	GPa
ZSZ 1	179
ZSZ 2	192
ZSZ 3	193
ZSZ 4	164
Shear Modulus	GPa
ZSZ 1	405
ZSZ 2	443
ZSZ 3	449
ZSZ 4	383
Poisson's ration	v
ZSZ 1	0.13
ZSZ 2	0.15
ZSZ 3	0.17
ZSZ 4	0.17

Table 2.4 (Continued)

Heat Capacity	J/g K
ZSZ 1	0.56
ZSZ 2	0.53
ZSZ 3	0.52
ZSZ 4	0.5
Thermal Conductivity	W/m K
ZSZ 1	98.32
ZSZ 2	95.83
ZSZ 3	86.29
ZSZ 4	74.01
Electrical Resistivity	$\mu\Omega$ cm
ZSZ 1	9.33
ZSZ 2	8.64
ZSZ 3	8.39
ZSZ 4	10.4

Out of these properties, the mechanical properties represent the strength of the material and its performance. For the feasibility by Electron Beam Melting, the properties of density, electrical, and thermal properties will be compared. If the properties of the proposed materials are concluded to be near the above-mentioned values, we can go ahead with the experimental phase. The combined properties of both the materials, in changing proportions are presented in table 3.4. ZSZ

denotes the ZrB_2 and $ZrSi_2$ ceramic, and the number 1, 2, 3, and 4 means 10 vol% $ZrSi_2$, 20 vol% $ZrSi_2$, 30 vol% $ZrSi_2$, and 40 vol% $ZrSi_2$ [50].

The heat capacity of all the mixtures is close to the thermal capacity of the Ti6Al4V alloy. However, the thermal conductivity is higher than the titanium alloy. The implications of the same will be studied by performing the experiments. Increasing the thermal conductivity by having the thermal capacity might result in the thermal energy being spread to the neighboring molecules and a decrease in the maximum temperature being attained. The density of the ZSZ powders is higher than the Ti6Al4V powder, which is advantageous as it will result in a decrease in the ‘smoke’.

On pre-heating the powder in the “jump-safe” and “melt-safe” process, the powder particles are lightly sintered together. This light connection facilitates in creating a complete electrical circuit and hence the values of the electrical resistivity presented in table 3.4 can be applied to the powder bed. This condition is helpful in validating the feasibility of manufacturing the UHTC powder using the EB-PBF process.

CHAPTER 3

MATERIAL PREPARATION AND EXPERIMENTATION

3.1 Powder characterization

The success of any powder metallurgical process depends to a great extent on the complete characterization and control of the metal powders. The method of powder production influences particle chemistry and structure, apart from the precise nature of particle size distribution [56]. Powder shape, packing density, flowability, impurities content, and particle size distribution are some of the key parameters that need to be tested prior to production. Particle shape controls the packing density and flowability of the powder. Accurate characterization of the powder particles aids not only for the prediction of the powder behavior in the EB-PBF process but also helps in scaling and adjusting the material properties in the mathematical model being developed.

3.1.1 Powder Particle Morphology

The raking system in the EB-PBF machine is responsible for spreading the powder evenly on the powder bed which is instrumental to high build rates and part accuracy. This is controlled by the powder flowability. The powder particle shape controls the flowability and is greatly increased if the powder shape is spherical or near-spherical. Such powder morphology is obtained from the Gas Atomization (GA) and Plasma Rotating Electrode Process (PREP). Powder packing density and compressibility also play an important role in determining the flowability of the powder. Thus, the powder particle morphology is an important factor to be considered in evaluating the quality of the powder and predicting the quality of the build in the electron beam powder bed fusion Process. The powder particle morphology of the powder bought and experimented in the EB-PBF is shown in figure 3.1 and 3.2. EDS analysis gives an idea about the chemical composition of the

starting powder. The presence of oxygen above a certain value can be detrimental for the entire process, resulting in oxygen scales build up on the top layer of the powder bed. Figure 3.3 and 3.4 are the EDS results of the starting powder. As seen in the SEM images, the powder shape is irregular, and the distribution seems wide. This is due to the inherent limitation of producing ZrB_2 and $ZrSi_2$. These compounds are made by chemical reduction and then mechanically ground to the required size. It can be seen in the figures that a significant amount of smaller particles are also seen attached to the powder particles. These smaller particles increase the susceptibility to electrostatically charging due to the increased surface area for their volume and can cause smoke in the process. Currently, obtaining spherical powder particles is difficult for the current material and hence it was decided to continue the experimentation process. It would not have been prudent to abandon such an intriguing topic due to the powder shape limitations. If the experiments in this thesis research provide any good results, the process for manufacturing spherical powder particles can be pursued.

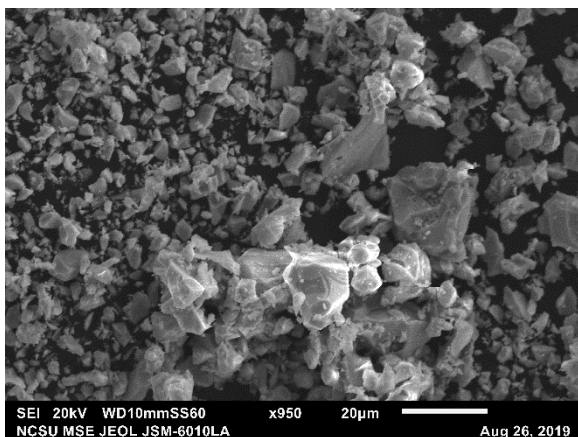


Figure 3.1 SEM imaging of ZrB_2 powder at 950x magnification.

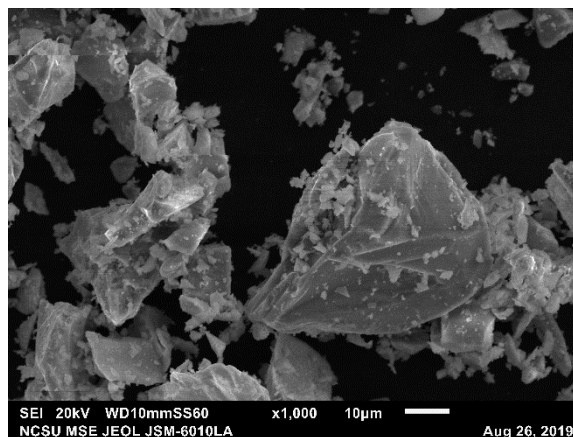


Figure 3.2 SEM imaging of $ZrSi_2$ powder at 1000x magnification.

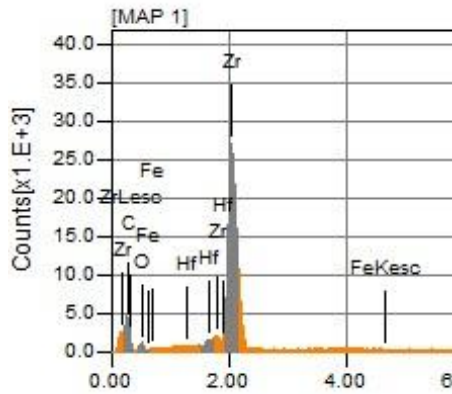


Figure 3.3 EDS analysis of the starting ZrB_2 powder.

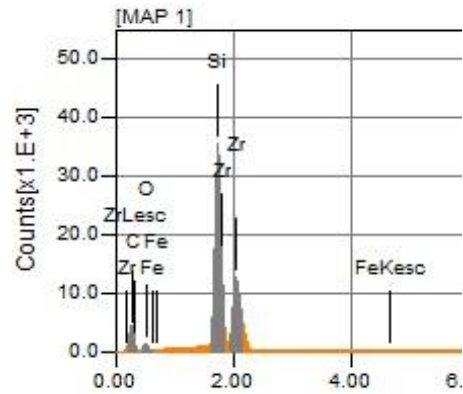


Figure 3.4 EDS analysis of the starting $ZrSi_2$ powder.

Also, Boron is not detected due to its lower excitation energy required to emit the X-rays on interacting with the electron beam. A trace amount of Hafnium is also detected in the powder mixture which might have resulted from the powder being manufactured in the same facility.

3.1.2 Powder Density

Powder density was evaluated using gas pycnometry to understand the effect on the powder packing and is useful to model the thermal properties of the powder bed. The thermal conductivity at elevated temperatures is dependent on the density of the material as seen in the following section of mathematical simulation. The density was determined using the gas pycnometry process. A sample of known mass is placed in one of two chambers of known volume, maintained at a constant temperature. Nitrogen is then added to the system. The resulting equilibrium pressures are used in conjunction with the ideal gas law, and Archimedes principle of fluid displacement, to determine the apparent density of the particles. The change in pressure is detected and the density is calculated from these values. The final value selected is an average of six tests as shown in figure 3.1. The average value is 5.6569 g cm^{-3} .

3.1.3 Particle Size Distribution

Particle Size Distributions (PSDs) were measured on a Microtrac S3500 with a sample delivery controller using the Fraunhofer laser diffraction method. The Microtrac operates on the principle of laser diffraction to measure the powder particle size. Two drops of a surfactant and a powder sample in the amount of ~1% of the volume of deionized water used for dispersion is added into the sample delivery controller. The delivery controller can ultrasonically agitate the solution if necessary, to break apart agglomerations of particles. The solution is then passed to a chamber within the Microtrac S3500 device, which is then impinged upon by a laser. The powder particles in the solution scatter the laser beam and the resulting angles of diffraction are detected to estimate the size of the powder particles. The advantage of this method is the large dynamic ratio, the range of the measurement that can be measured in one sample. The divergence of the samples is detected using a photodiode detector array. There is an inverse relationship between the particle size and the angle of diffraction. The intensity of the diffracted laser is also affected by the particle size. The intensity decrease is proportional to the square of the particle diameter [57]. The limiting factor for the powder particle size detection is the laser wavelength.

Table 3.1 Results of the Pycnometer density measurement.

Run	1	2	3	4	5	6
Density (g/cm³)	5.6593	5.6586	5.6555	5.6617	5.6525	5.6535

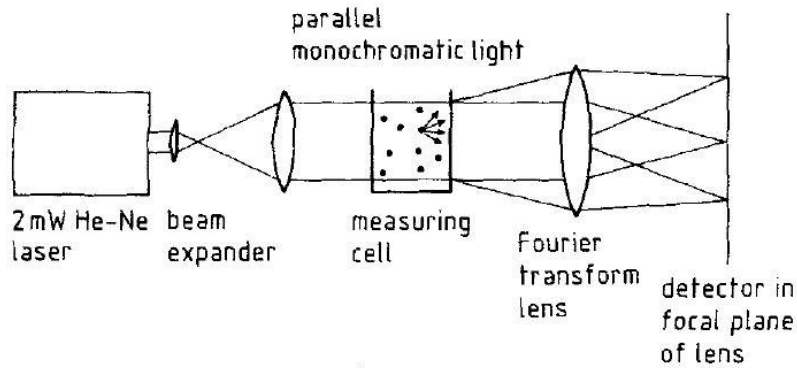


Figure 3.5 Laser diffraction powder measurement based on the Fraunhofer diffraction principle [58].

Based on the Fraunhofer's principle, the diffraction is only affected by the particle dimension, with the other configurations being kept constant. The method of laser diffraction is based on the assumption that the powder being analyzed is perfectly spherical. If the particle is not spherical, then the orientation of the particle at the time of laser impingement is measured. The measure is a rough estimate of the size distribution of non-spherical particles being analyzed. The Microtrac computational software determines the results for the test. The plots for the results are attached as figures 3.6 and 3.7. The PSD results are presented in number and volume distributions. Volume distributions are biased against the larger particles. A large particle has a higher volume compared with numerous smaller particles where the radii of the particles add up to the radius of the large particle. Relying solely on the volumetric data can be misleading for estimating its behavior in the machine. A number distribution allows the true amounts of each size of particle to be seen, and a shift to the left is observed in the S-curve that is plotted for the cumulative count.

Zirconium based powders are produced using the chemical process involving oxide-reduction processes and then mechanically treated to decrease the size. However, experimentation was

carried out with irregularly shaped particles due to the advantages associated with the production of UHTCs with the EB-PBF process. Future technology development involving spherical production of Zirconium based powders will result in better production of UHTCs using this process.

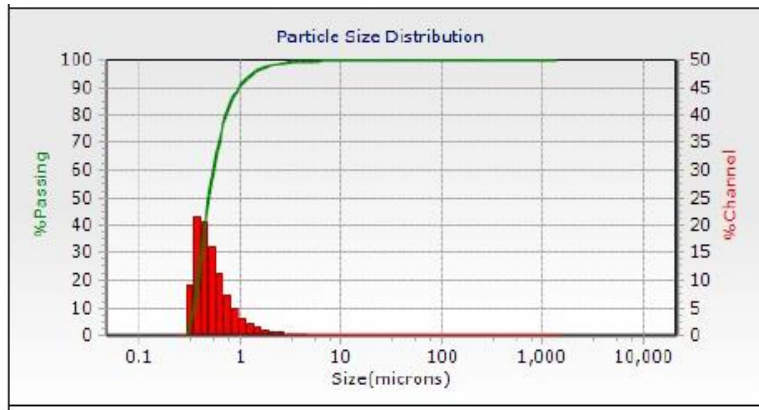


Figure 3.6 Numerical size distribution of the UHTC powder combination experimented.

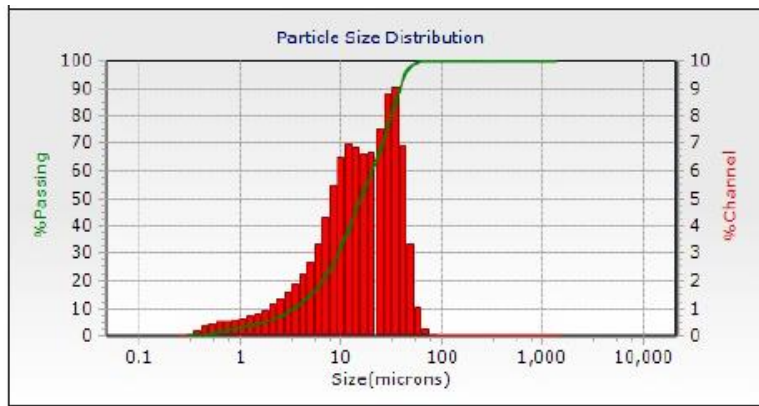


Figure 3.7 Volumetric size distribution of the UHTC powder combination experimented.

The supplier-provided powder size of ZrB_2 and $ZrSi_2$ is 45 to 106 microns and the number and volume data follow a similar trend. The powder has a higher amount of fines in the powder. This is not evident from the volume distribution but can be seen in the number. Percentage range d10 - d90 is the industry standard of presenting the powder size data. Smaller and larger particles are typically produced even in well-controlled powder development processes and manifest as low-

intensity tails at the ends of the graph. Therefore, these tails are not reported and three values, d10, d50, and d90 in microns are reported in table 3.2.

Table 3.2 Results of the MicroTrac Laser Diffraction.

Powder Sample	d10	d50	d90
ZrB ₂ – 30 vol% ZrSi ₂	2.924	24.35	49.39

3.2 UHTC Sample preparation for EB-PBF Process

Manufacturing UHTCs using the EB-PBF process has never been done before, and hence precautions were taken to ensure safety and to avoid any hazardous outcomes due to the interaction of the electron beam with the ZrB₂ and ZrSi₂ powders. In the Electron Beam Melting process, the first step is pre-sintering the powder using defocused electron beams to initiate the necking among the particles. Necking ensures a better path for electrical conductivity in the complete electrical circuit, and this additional bonding helps in dissipating any charge build-up on the top layer due to the electrostatic interaction of the beam and the loose powder in the top layer. Local bonding also increases the mass of the joined powder particles, and the gravitational force acting on this group overcomes the electrostatic repulsion arising due to charging, and thus preventing smoke. Zirconium powder is explosive in nature and interacting with a high energy-dense electron beam can result in highly exothermic reactions. To counter the problem of smoke and unwanted disruption in the EB-PBF machine, the powder was lightly pressed in a hydraulic press and then it



Figure 3.8 Pucks pressed at 8 MPa for 5mins, *Figure 3.9* Pucks placed in the Stainless-
ready to be heated. Steel baseplate at CAMAL

was loaded into a machined stainless steel plate specifically for the Arcam S12 EB-PBF Machine, at CAMAL. The powder was mixed in predefined quantities of ZrB_2 and $ZrSi_2$, and then it was ball milled to ensure proper mixing of the powders. The powder was pressed into the shape of circular disks of 1 inch in diameter and 3.5 mm thick, using Ethanol as a binder to impart green strength during handling. Pressure of 8 MPa was applied for 5 minutes to lightly bond the powder particles together. The pressed and shaped powder pucks were then heated to a temperature of 1000 °C for three hours in an inert environment of Argon gas. The resulting shape was a fragile and delicate powder puck of $ZrB_2 - 30 \text{ vol\% } ZrSi_2$, which were placed in the prepared baseplate and loaded into the EB-PBF machine. 6 pucks were successfully prepared and placed into the baseplate. This process ensured that the powder particles did not result in smoke on impinging

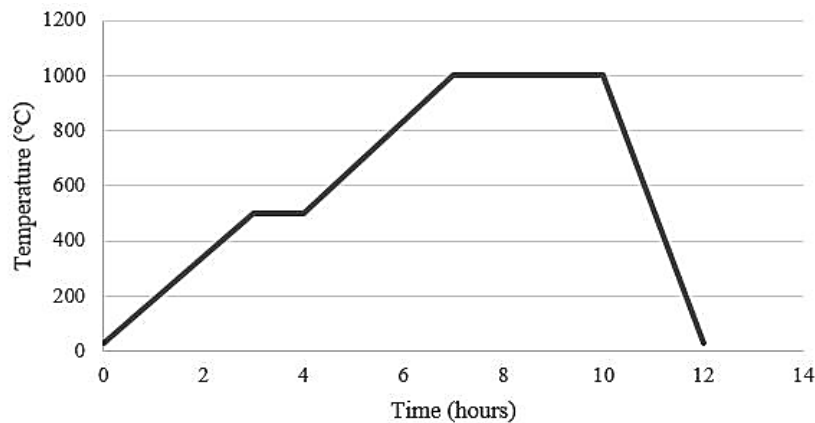


Figure 3.10 Temperature profile for heating the pucks in the furnace

with the electron beam. The prepared pucks are shown in figure 3.8 and 3.9. The temperature profile used in the furnace is shown in figure 3.10.

3.3 Experimentation

Experiments were planned on the $ZrB_2 - ZrSi_2$ pressed pucks to study the effects of UHTC interaction with the high-intensity electron beam. The experiment was performed on the Arcam

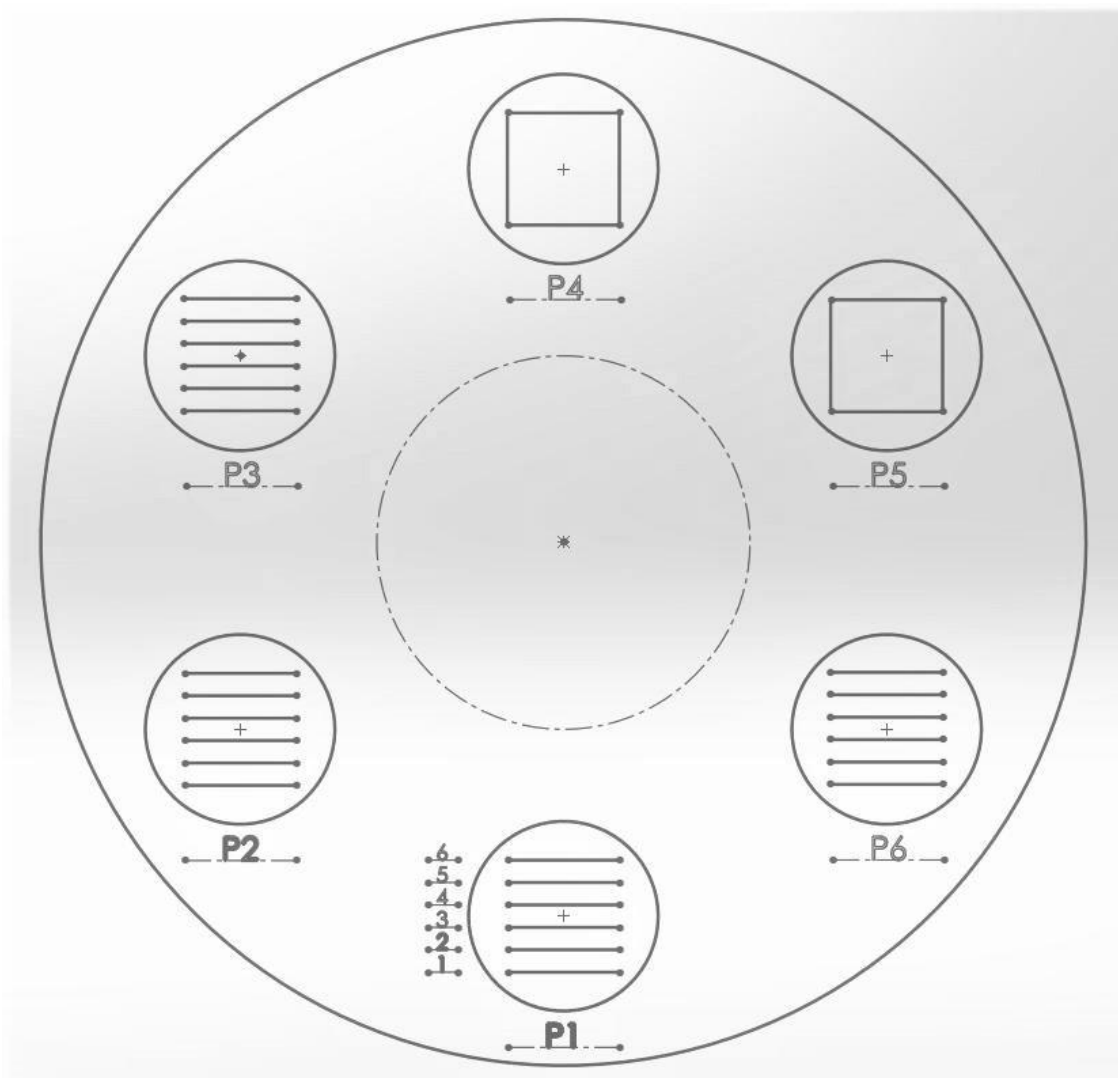


Figure 3.11 Layout of the 1D tracks planned for $ZrB_2 - 30 \text{ vol\% } ZrSi_2$ pucks placed on the stainless-steel baseplate placed in the EB-PBF machine.

AB S12 EB-PBF machine at the Center of Additive Manufacturing and Logistics (CAMAL) at the North Carolina State University. The process parameters were planned based on the results generated from the FEA model described in the next chapter. Two types of tests were planned, 24 one dimensional melt tracks and two square hatchings on the pucks. The entire assembly was heated to 800 °C by hatching a square pattern using a defocused electron beam on the center region of the stainless-steel plate as shown in figure 3.11 from a starting temperature of 25 °C. The heating step was planned to simulate the pre-heating step of the EB-PBF process and was included in the mathematical model. Square hatching by a highly focused beam was carried out to increase the surface temperature of the pucks to the pre-heat temperature, which was monitored by the infrared camera. The chamber was initially depressurized and a vacuum of 10^{-4} Torr was created with Helium gas to create an inert atmosphere. Out of the six pucks, single dimension melt tracks were planned on four pucks and square hatching patterns were planned on the remaining two pucks. 6

Table 3.3 Process parameters for the planned melt tracks on the pucks as per figure 3.11.

Puck No.	Track no.	Beam power (W)	Beam scanning speed (mm/s)	Line energy (J/mm)
P1	1	500	250	2
	2	500	500	1
	3	500	750	0.667
	4	500	1000	0.5
	5	250	100	2.5
	6	300	100	3

Table 3.3 (Continued)

P2	1	1000	250	4
	2	1000	500	2
	3	1000	750	1.333
	4	1000	1000	1
	5	2000	250	8
	6	2000	500	4
P3	1	2000	750	2.667
	2	2000	1000	2
	3	2500	750	3.33
	4	N/A	N/A	N/A
	5	250	150	1.667
	6	300	150	2
P4	1	300	100	
P5	1	300	150	
P6	1	1500	250	6
	2	1500	500	3
	3	1500	750	2
	4	1500	1000	1.5
	5	2500	250	10
	6	2500	500	5

tracks of 15 mm length were planned, and two squares of 15 mm each were planned on two of the pucks, resulting in 24 different process parameter combinations that can be tested for this UHTC powder combination.

The accelerating voltage in the electron beam gun is kept constant at 60 kV and the variation in the electron beam power is done by changing the beam current. Thus, the electron beam current and beam scanning speed was input into the build file for the machine. Electron beam spot size was 200 microns in radius. Hatch spacing of 0.1 mm was taken as the hatch spacing for the two square hatch in P4 and P5 puck. The process parameters input is shown in table 3.3. Puck 3 Run 4 was not executed due to the electrode gun arc tripping. The electron beam current executed was a bit less than the input value due to the high-power requirements and these were extracted from the log files and used to simulate the mathematical model. The chamber setup and the equipment attachments are shown in figures 3.12 and 3.13.

The processed pucks were cooled in the machine for more than twelve hours and the removed pucks were then analyzed using a Confocal Laser microscope and the Scanning Electron Microscope. The laser microscope aided in determining the width of the Heat Affected Zone

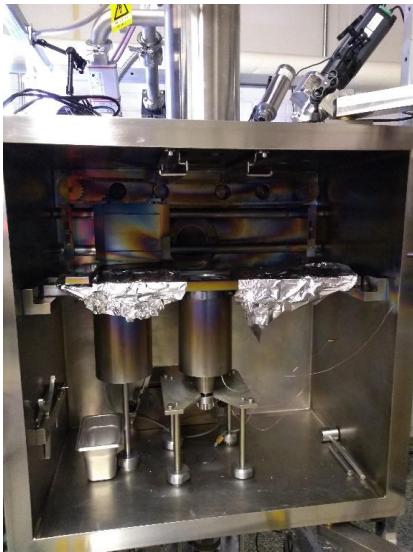


Figure 3.12 Inside view of Arcam S12 set up for the experiment.



Figure 3.13 Thermal camera and pyrometer attached to the top of the Arcam S12.

(HAZ) of the processed tracks on the pucks and was compared with the results of the FE model simulations. SEM images were used to detect the occurrence of recrystallization in the tracks and to know if $ZrSi_2$ melts and engulfs the unmelted ZrB_2 to form a solid network. Successful results have been obtained for metals with additives to follow a similar behavior [44], [59]. Higher energy intensity in the HAZ for a longer amount of time might result in crack formation and the same will be kept in mind when analyzing the high beam power melt tracks. Surface roughness will be measured for the process's tracks and the maximum dimensions for the melt consolidations of the surface will also be noted. These data will help in evaluating the process parameters for the processing of ZSZ composites.

The conduction of the experiment confirmed a few critical points for testing the feasibility of manufacturing ZSZ using EB-PBF process:

- The pressed pucks with the proposed combination of ZrB_2 and $ZrSi_2$ did not 'smoke' on interacting with the high-intensity electron beam. This has paved the pathway for future research in UHTC manufacturing using the EB-PBF process.
- The powdered pucks are electrically conductive and ensuring the flow of electrons to the ground to complete the circuit, and hence the values of electrical conductivity for the bulk UHTC processes with traditional sintering techniques can be used as a reference for testing the feasibility for EB-PBF processes.

CHAPTER 4

MATHEMATICAL MODELING OF ELECTRON BEAM MELTING FOR UHTC

During the electron beam melting (EB-PBF) process, electrons transfer their kinetic energy to the atoms via collision until their energy lowers below the threshold energy. These collisions increase the internal energy of the powder particles that result in an increase in the local temperature. The material microstructure and properties of the consolidated parts strongly depend on the starting powder composition and the processing condition [27], [35]–[38]. Finite Element Modeling of the Electron Beam Melting techniques involves determining the governing equations and solving the same using computational techniques. Most EB-PBF fabrication research and development have been focused on high-performance metallic materials, such as copper, aluminum, tool steel, titanium alloys, etc. Since the mathematical modeling of the UHTCs for manufacturing using Powder Bed Fusion processes has never been done before, existing modeling and simulation tools will be helpful in the implementation of the proposed UHTC-based ceramics to understand the process.

Before experimenting with the proposed materials, computer simulations were carried out based on the developed Finite Element (FE) method. The aim of this FE Analysis was to select the optimum combination of process parameters for adequate HAZ dimensions during experimentation. Galati et. al [25] have presented an exhaustive review on the mathematical models applied to Electron Beam Melting (EB-PBF) process. Numerous attempts have been made in determining the manufacturing process parameters for developing new materials for EB-PBF involving the trial and error approach. Developing a finite element model and carrying out simulations results in saving time and expenses, as running the electron beam machine is expensive

and considerable amount of time goes in setting up an EB-PBF machine to test new materials. The advantage of implementing the finite element models in this research was exploited, and numerous process parameter combinations were studied to determine the set that had the highest potential to manufacture UHTCs using the EB-PBF process. Process parameters that have successfully resulted in dense parts for metals served as the starting point for conducting simulations. The temperature profile is generated in the model and the distribution of the temperature gave an approximation of the behavior of the UHTC powder, and 24 process parameters were selected and fed in the Arcam EB-PBF software and experimented on the prepared pucks.

4.1 FEM Models for EB-PBF process

The advent of the electron beam melting techniques is relatively newer as compared to Laser Beam Melting and other additive processes. Mathematical models with different levels of assumptions are being developed to replicate the actual physical phenomenon taking place in the powder bed. The level of complexity in the model is affected by the available computational power and the capability of the solver. The mathematical modeling can be broadly classified as coupled and uncoupled models depending on the method adopted by the researchers. In this research, a mathematical model has been developed to predict the temperature distribution in the powder bed under the influence of the traversing electron beam. The results of the mathematical model will be compared with the experimental results. The summary by Galati [25] served as one of our main references, which explains that uncoupled thermal models assume the thermal transfer from the electron beam to take place via conduction among the powder particles in the unsintered layers, from the unsintered layer to the sintered layer and downwards through radiation in the chamber. Uncoupled models are limited to approximating the thermal behavior of the material layer under

the electron beam, and the interaction of the liquid HAZ with the electron beam, surrounding powder particles, and the solidified layer is not considered. This result is not a complete representation of the actual process but provides a strong base to select the process parameters and serves the purpose.

Three different models exist for the simulation of a physical process: black box, grey box, and white box model. The models are distinguished depending on the level of approximations formulated in each. Black-box models have high level of assumptions. The mechanism behind the physical process is not fully represented in the system and so, the results generated are not accurate. However, these models require the least amount of computational time and are cheap, and so are relied upon by various authors as an initial step for an approximation when experimenting with new process parameters or materials. White-box models are modeled accurately involving all the mechanisms to their maximum level possible and thus the level of approximation in this model is minimal. They generate the most accurate result but require extensive computational time and resources and are expensive. Only a few research groups and national labs have succeeded in implementing models with such a high level of fidelity. Established materials like Ti-6Al-4V, IN 718, CoCr, etc. have finite element models available with high fidelity due to their extensive usage in the industry and years of research conducted on the behavior of these metal alloys in the EB-PBF machine.

One of the methods for formulating a black box model is treating the powder bed as a continuum to approximate the process and simulating the transient thermal process on the block. However, the primary concern is the representation of the powder properties as applied to the continuum

phase in an FE model. The heat transfer due to conduction in the model is the primary source of heat transfer in the powder bed. The electron beam melting process takes place in the vacuum and so the heat transfer due to convection from the powder bed to the chamber is absent and can be neglected. Thermal energy transfer also takes place due to Marangoni convection and viscous forces, however, these complex mechanisms are neglected by various authors in the black box model. Emissivity and the heat transfer due to radiation at the top surface and in the powder bed have been neglected by a few authors [36], [38], however, it is critical in determining the thermal conductivity of the powder bed. In the powder bed, the thermal energy transfer takes place due to conductivity at contacts and radiation. This has been formulated in the model, which is described in the subsequent sections. Emissivity at the top layer has also been considered to model the radiation heat loss arising in the chamber.

The parameters that control the quality of the build are beam power, beam scanning speed, beam size, hatch spacing, layer thickness, preheat temperature, scanning strategy, scanning mode, number of outer contours, etc. Initial experimentation is done for single dimension melt tracks for developing the process parameters for a novel material, and the process parameters being manipulated are electron beam power and beam scanning speed. The process parameters that can be manipulated to generate a set of single dimension experimentation parameters are limited for one dimensional processing of electron beam melting. It has been found from the literature review that the experimentation investigations involve the use of parameters such as energy density and line density. Energy density is the ratio between the power and the section of the beam. Line energy is the ratio of beam power to the scan speed [36]–[38]. The effect of varying the electron beam

power, scanning speed, and hence the line energy density has been studied in this research, and the results have been presented in the results section of the thesis.

4.2 Material properties for ZrB₂ – 30 vol% ZrSi₂

The mathematical modeling proposed by Zäh and Lutzmann [36] treats the energy transfer from the electron beam to the powder bed as a Gaussian distribution function which gives the intensity distribution as a function of the standard deviation, similar to the mathematical modeling of a welding heat source. The thermal conductivity of the powder bed is different from the thermal conductivity of the solid bulk material and needs to be modified. The porosity in the powder bed behaves as an insulator and inhibits the thermal energy transfer to increased depths in the powder bed.

Different strategies were adopted to determine the thermal properties of the powder bed and the properties for each temperature values were determined by calculating the function presented by various researchers. Numerous calculations have been carried out for determining the thermal properties of powder beds for metals, however, similar computations have not been done for ceramic powder beds. ZrB₂ finds usage in various applications and has been mixed with various other ceramics and metals to produce composites with exceptional properties that have found usage in production processes, aviation, space-vehicles, defense, etc. The ease of manufacturing ZrB₂ for simple geometric shapes like cuboids, tiles, and cylinders has resulted in the thermal properties being studied and published by various authors. The initial step was to determine the correct thermal conductivity of bulk ZrB₂. These properties can be studied further from the works of Zimmermann [60], who has conducted experimental studies on the required properties. Another work following it closely is the dissertation by McClane [61]. McClane has worked on reporting

the thermal properties of Zirconium and other transition metal borides solid solutions. As reported by them, the temperature-dependent thermal conductivity can be arrived at by using the following equation

$$k(T) = \rho(T) C_p(T) \alpha(T) \quad (1) [61]$$

Where $k(T)$ is the temperature-dependent thermal conductivity, $\rho(T)$ is the temperature-dependent density of the material, $C_p(T)$ is the temperature-dependent heat capacity of the material and $\alpha(T)$ is the temperature-dependent thermal diffusivity of the material. Zimmermann gave the following equation to calculate the density which uses the measure thermal strains as the parameter that affects the density change with temperature. For ZrB_2

$$\rho(T) = \rho_{300K} \left[1 + \frac{\Delta l(T)}{l_{300}} \right]^{-3} \quad (2) [60]$$

$$\left(\frac{\Delta l}{l_0} \right)_{ZrB_2} = -1.64 * 10^{-3} + 4.92 * 10^{-6} T + 1.72 * 10^{-9} T^2 - 2.31 * 10^{-13} T^3 \quad (3) [60]$$

where $\Delta l/l$ is the thermal strain of the material. The values followed by McClane were of Touloukian [62], who presented a different approach which is as follows,

$$\rho(T) = \rho_{300K} \left[1 + \frac{\Delta l(T)}{l_{300}} \right]^3 \quad (4) [62]$$

$$\left(\frac{\Delta l}{l_0} \right)_{ZrB_2} = -0.135 + 3.490 * 10^{-4} T + 2.390 * 10^{-7} T^2 - 3.976 * 10^{-11} T^3 \quad (5) [62]$$

The values for both the equations were evaluated and a comparison of them is presented as figure 4.1. The same values are used with a room temperature density of 5.6569 g cm^{-3} were used as a reference. The plot for the temperature-dependent density is presented as figure 4.2.

As can be seen from the graph, both the values were in proximity to each other and start to diverge at a higher temperature. The Zimmermann model was implemented in this thesis. Heat Capacity was determined using the NIST-JANAF [63] tables for ZrB₂, which was followed by both Zimmermann and McClane. The NIST-JANAF empirical relation is as follows:

$$C_p = 66.96241 + 5.665010 * t + 1.433879 * t^2 - 0.151665 * t^3 - 1.83599 * t^{-2} \quad (6) \quad [48]$$

Where, $t = T/100$. This will generate the results in $J \text{ mol}^{-1} \text{ K}^{-1}$ unit, which needs to be divided by the Molar Mass of ZrB₂ which is $1112.8 \text{ g moles}^{-1}$. The generated result with the same is presented in figure 4.3. Zimmermann has presented the thermal diffusivity of ZrB₂ that was measured experimentally, and curve fitting methods were used to fit the data which is not presented. The temperature-dependent specific heat capacity of ZrSi₂ has not been studied exhaustively and reliable values were not available. Hence, the values of ZrB₂, which is in more proportion as

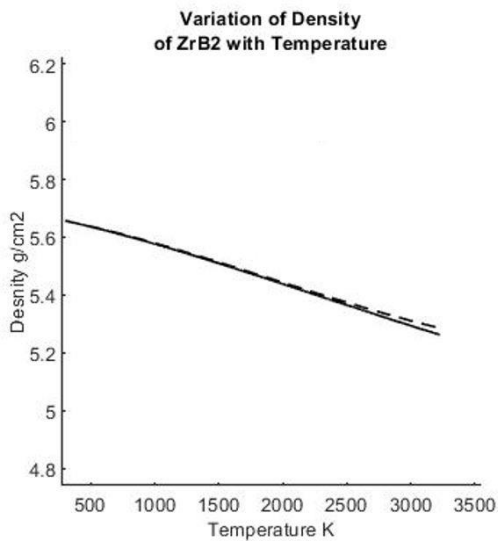


Figure 4.1 Comparing the results of Zimmermann and Touloukian for thermal expansion strain.

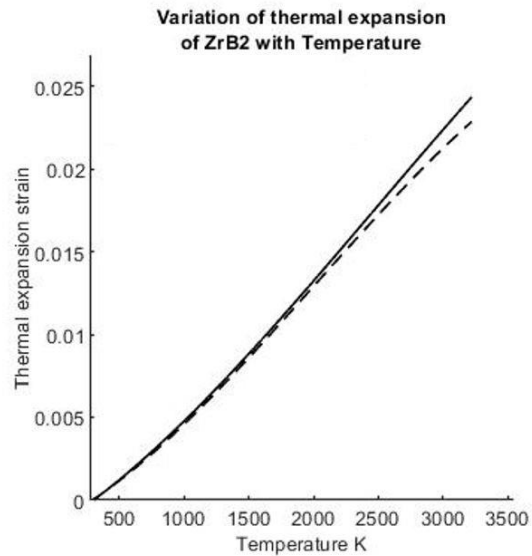


Figure 4.2 Comparing the results of Zimmermann and Touloukian for density.

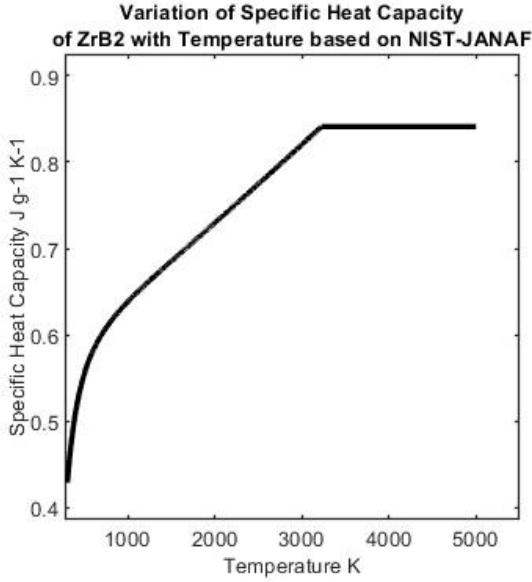


Figure 4.3 Variation of the specific heat capacity with temperature based on NIST-JANAF tables.

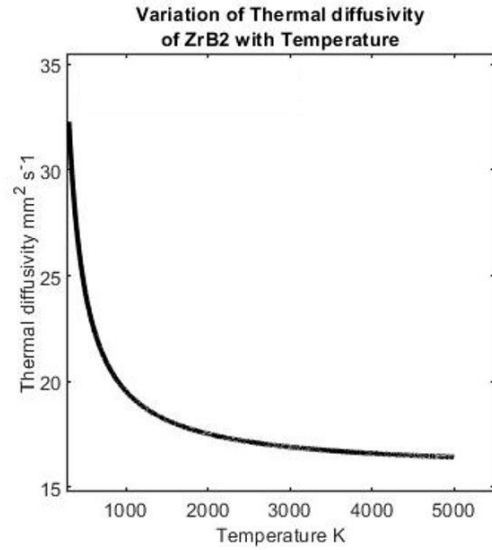


Figure 4.4 Variation of thermal diffusivity based on the work by McClane.

compared to ZrSi_2 , is defined as the material property for the model with a peak being inserted to include the latent heat of fusion for the melting of both the materials. McClane also conducted the same study and presented an exponential empirical formula for the calculation of the same, which is as follows

$$\alpha = a e^{b/T} \quad (7) [61]$$

Where a is $0.1572 \text{ cm}^2/\text{s}$ and b is 215.85 K . The values of the thermal diffusivities are plotted in figure 4.4. With the three parameters computed, the value of thermal conductivity can be calculated using equation (1). The results are plotted in figure 4.4 and the room temperature value of thermal conductivity of $86.82 \text{ W m}^{-1} \text{ K}^{-1}$. These results are supported by the results of McClane and also by the work of Nakamori [64]. It is well known that the electrical conductivity takes place by the transfer of energy due to electron phonon interactions in the system. Weidemann-Franz Law is

used by the author to compute the effect of thermal conductivity due to electron transfer. It was concluded by both the papers that the thermal conductivity due to electrons is a major contributor and the effect of phonons is minimal. Zimmermann provided the details for a straight line depicting the electrical resistivity with a room temperature value of $22 \mu\Omega \text{ cm}$ and a slope of $0.045 \mu\Omega \text{ cm K}^{-1}$. There is a discrepancy found in the results of Zimmermann and McClane for the thermal conductivity due to electrons, but the final values are close. The thermal conductivity due to electron energy transfer is responsible for the energy transfer in the liquid phase and this value is to be used when the powder melts to form a liquid pool. The emissivity of the powder particles regarding interaction among the particles is handled by the Tolochko equations. For the emissivity of the top layer of the powder bed, the equations presented by Sih and Barlow [65] have been used. Using their formulation, an emissivity of 0.91 is considered for the top layer of the powder bed. The thermal conductivity is determined by equation (1) presented earlier. The thermal conductivity of bulk ZrSi_2 is determined by Samsonov [66], and the temperature dependent conductivity follows

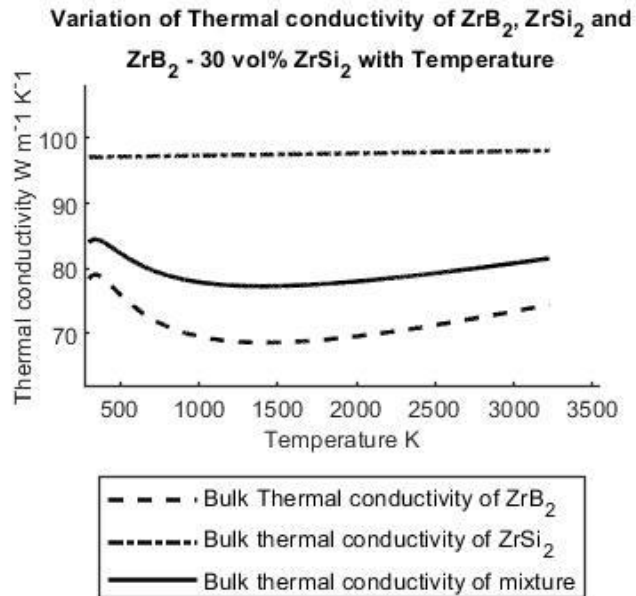


Figure 4.5 Comparing the thermal conductivities of bulk ZrB_2 , ZrSi_2 , and the proposed combination of $\text{ZrB}_2 - 30 \text{ vol}\% \text{ ZrSi}_2$.

the trend as represented in equation (8), where t is the temperature divided by 100, and conductivity is obtained in $\text{W m}^{-1} \text{K}^{-1}$.

$$k(T) = 97 + 3.46 \times 10^{-4} t \quad (8) [66]$$

Computing the thermal conductivity, the resulting values are presented in figure 4.5. The combination of both the materials is done using the rule of mixtures. The next step is to include the effect of porosity in computing the thermal properties for the model. The temperature dependent properties of the material combination under investigation are also listed in table 4.1.

Table 4.1 Temperature dependent properties of $\text{ZrB}_2 - 30 \text{ vol\% ZrSi}_2$.

Temperature (K)	Thermal conductivity ($\text{W m}^{-1} \text{K}^{-1}$)	Specific Heat Capacity ($\text{J g}^{-1} \text{K}^{-1}$)	Density (g cm^{-3})
300	83.964	0.429	5.657
500	82.315	0.557	5.636
700	79.735	0.601	5.614
900	78.292	0.628	5.589
1100	77.565	0.649	5.564
1300	77.276	0.668	5.537
1500	77.270	0.686	5.510
1700	77.456	0.704	5.481
1900	77.777	0.721	5.453
2100	78.198	0.739	5.424
2300	78.693	0.757	5.394
2500	79.243	0.775	5.365
2700	79.835	0.793	5.336
2900	80.458	0.811	5.308
3100	81.105	0.830	5.280
3200	81.435	0.839	5.266

3.3 Effect of porosity on the thermal properties

Various models have been presented by researchers to calculate the value of porosity, and some researchers have assumed the value to save computing time and facilitate near-approximate results. The proposed methods of determining the values of thermal conductivity of the powder bed are chiefly differentiated into two approaches,

1. Treating the powder bed as powder particles floating in a fluid bed of gas
2. Combining the heat transfer due to conduction at contacts and radiation in the voids neglecting the presence of any gas.

Since the process takes place in a chamber pressure of 10^{-4} Torr, option 2 is the closest approximation to the process occurring in real-time. Hence, we will follow process 2 in this research.

Reference papers for the same were referred to get the density values for a powder bed. Cheng and Chou [38] assumed a porosity level of 50% for their powder bed. Romano et al. [67] assumed a porosity value of 30% for the powder bed. The *Zehner/Bauer/Schlünder* [68] (ZBS) model also suggests that packed beds have a porosity value between 0.40 and 0.42 for equally sized spheres. Qi et al. [34] assumed a relative density of 64% for their simulation. Dong et al. [69] assumed a porosity of 50% for the powder bed. However, a better approach was found to be used by other authors. They assumed a specific packing pattern for the powder beds, involving Simple Cubic (SC) arrangement, Body Center Cubic (BCC) packing, and Diamond-shaped body packing arrangement. Tolochko et al.[70] gives a relative density of 68% for BCC packing and 52.4% for SC packing. Galati et al. [37] assumed BCC packing and considered a relative density of 68% for the powder bed. Following the raking action in the Powder Bed Fusion, we can assume the powder

bed density to be the same as BCC, which is 68%. The equation for a poly-dispersed powder phase in a fluid bed, as discussed in option 1 above, can be found using the equation 6.3 of VDI Heat Atlas [71] that depends on the powder size spread. The ZBS model has assumed a BCC packing of the powder and hence a porosity of 32%. Helium gas was used as the inert medium during experimentation, and hence for the ZBS model, Helium was used as the fluid medium in which the powder particles are dispersed.

The temperature-dependent thermal conductivity of Helium was used as the thermal conductivity of the matrix phase in the upcoming calculations. The calculations of the ZBS model gave the thermal conductivity of the powder bed. Equations 9 to 11 are implemented to determine the thermal conductivity of the powder bed with option 1, where k_{bed} is the thermal conductivity of the powder bed, λ_p is the thermal conductivity of the powder particle, λ_f is the thermal conductivity of the fluid, ψ is the porosity, k_p is λ_p/λ_f , and B is the deformation parameter.

$$k_{bed} = 1 - \sqrt{1 - \psi} + \sqrt{1 - \psi} * k_c \quad (9) [68]$$

$$k_c = \frac{2}{N} \left(\frac{B}{N^2} \frac{k_p - 1}{k_p} \ln \frac{k_p}{B} - \frac{B + 1}{2} - \frac{B - 1}{N} \right) \quad (10) [68]$$

$$N = 1 - \left(\frac{B}{k_p} \right), B = 1.25 \left(\frac{1 - \psi}{\psi} \right)^{\left(\frac{10}{9} \right)} \quad (11) [68]$$

Implementing this equation, we get the value of the thermal conductivity of the bed as plotted in figure 4.6. This method has also been used to accurately determine the thermal conductivity of powder flow [72] and hence can be applied to stationary powder beds as well. To gather the thermal conductivity of the lightly sintered powder bed, the method proposed by Tolochko [70] was best suitable. There is a drastic change observed in the value of the thermal conductivity. Galati et al.

have assumed the thermal conductivity of the powder bed similar to Tolochko considers two different heat transfer mechanisms, due to radiation as shown in equation (12) and due to the necking as shown in equation (13), that are formed due to touching of the spheres.

$$\lambda_{rad} = \frac{16}{3} l \sigma T^3 \quad (12) [70]$$

Tolochko has concluded that the mean free length l of the photons is of the order like the pore size, which can be assumed to be like the particle size. Considering a particle size of $70 \mu\text{m}$, and σ is the Stefan Boltzmann constant, the value of this was computed. The heat transfer due to conduction through the area of contact can be taken as

$$\lambda_c = \Lambda \lambda_0 x \quad (13) [70]$$

Where, Λ is the normalized constant, which is 1.732 for a BCC packing and, λ_0 is the thermal conductivity of the bulk material and x is the relative size for contact which is 0.09. The total thermal conductivity of the powder bed is a summation of both the above values and is shown in figure 4.6. With increasing temperature, the heat transfer due to radiation increases, and due to conduction at the necking reduces. In the liquid stage, the heat transfer due to radiation is not prevalent and the heat transfer due to electron activity is the only phenomenon that is modeled in

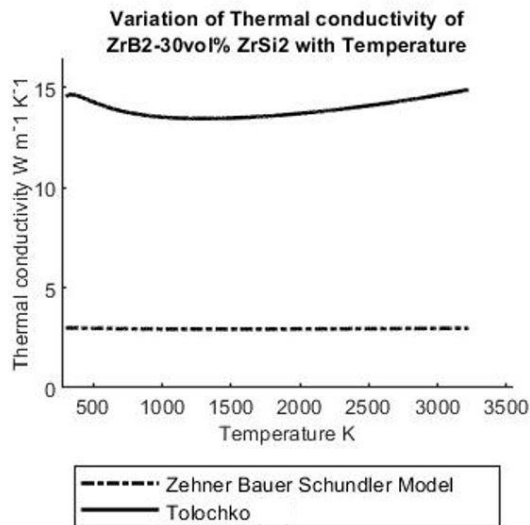


Figure 4.6 Temperature-dependent thermal conductivity of the powder bed.

the system. Heat transfer due to Marangoni convection, viscous and capillary forces, etc. are also present in the process in real time, however, computing these processes is expensive and requires high processing capabilities. These were ignored in the current model being developed and will not result in any changes in the thermal model. The specific heat of the powder is kept the same as the specific heat of the solid bulk material, and the same is supported by numerous authors [22], [36]–[38], [70].

3.4 Modeling the heat source for Electron Beam Melting

To account for the latent heat of fusion during melting, the same is converted to a value of specific heat for the change over a unit temperature, which results in a spike on the plot. Two spikes are fed into the model, one for the latent heat of fusion for ZrB₂ and the other for ZrSi₂. This method of adding a spike to the data of the specific heat dates to the mathematical modeling papers for welding and was used by Goldak [73] in his model. Rosenthal [74] used a moving point source for modeling the heat source. Friedman [75] and Goldak used an elliptical model, with Goldak using an asymmetric model to incorporate the effects of position and velocity of the arc.

The analysis was carried out to simulate a moving heat source of constant heat flux over a straight line on the top surface of the powder layer, and the temperature variations of the HAZ were noted. The analysis was carried out in ANSYS with the moving heat source modeled as a Gaussian distribution as follows

$$q = \bar{P} e^{-\frac{[(x-x_0)^2 + (y-y_0)^2 + (z-z_0)^2]}{r^2}} \quad (2)$$

Where, q is the heat flux, \bar{P} is the beam power intensity absorbed, r is the beam radius, (x,y,z) is the co-ordinate at the location of heat flux distribution, (x_0,y_0,z_0) is the instantaneous center on the

path of moving heat source. The analysis was carried out initially by varying two process parameters: beam velocity and beam power; by changing one and keeping others the same. The parameter steps were selected by taking the analysis values of Zäh and Lutzmann as a reference, but the values of power and scan speed were increased by a factor as even though ZrB_2 would not be melted, it will conduct the thermal energy and hence additional power needs to be supplied so that $ZrSi_2$ retains the heat for enough time to melt. The absorption of the electron beam in the powder layer is modelled as per the value mentioned in the work of Körner et al. [32]. The choice of the heat flux model as a surface heat flux or a volumetric heat flux does not result in significant changes in the HAZ dimensions [76].

The initial set of experimentation were performed to analyse a single melt track on the powder bed, as the powder being analysed is a ceramic powder, never been manufactured before. Single melt tracks provide insight into the primary process parameters, electron beam power and scanning speed, as a starting location for determining the entire gamut of parameters [77], [78]. To avoid situations like smoke and as a precaution measure, single tracks are preferred. Also, the powder is not directly loaded into the machine, rather it is pressed and then placed into mould created for it. Further details have been discussed in the experimentation section. ANSYS simulations are carried out for the single run melt tracks. The beam power and scan speed analysed are 500W, 1500 W, 2000W, 2500W and 250 mm/s, 500 mm/s, 750 mm/s and 1000 mm/s. To also consider the outcome of low beam power at low beam speed, beam power of 250W and 300 W were also analysed at 100 mm/s and 150 mm/s respectively. A preheating condition of 800 °C was applied to simulate the pre-sintering process that takes place in the Arcam EB-PBF machine.

CHAPTER 5

RESULTS AND DISCUSSION

5.1 Simulation results

The simulations were run for a wide variety of process parameters ranging from beam power of 500 W to 2500 W, and the beam scanning speed of 500 mm/s to 1000 mm/s. Four cases of 250 W and 300 W beam power with a scanning speed of 100 and 150 mm/s were also experimented. The starting parameters were initially selected from the publications of Ti-6Al-4V since $ZrSi_2$ has the melting point in the similar range as the metal alloy. ANSYS Workbench Transient Thermal module was used to simulate the process. The solid model analyzed is shown in figure 5.1. In this model, three layers were modeled to represent the real-time setup of the process. The top layer is the $ZrB_2 - 30 \text{ vol\% } ZrSi_2$ powder, the middle layer is the bulk $ZrB_2 - 30 \text{ vol\% } ZrSi_2$, and the bottom layer is modeled as Stainless Steel. The cross-sectional area is $10 \text{ mm} \times 10 \text{ mm}$, and the layers are 0.1, 1, and 1 mm in thickness. On the top surface, a line of 5 mm is sketched that acts as a path for the electron beam, and the constant velocity traversing is simulated by dividing the entire path into 200 steps and the heat input is held at a particular point depending on the scanning

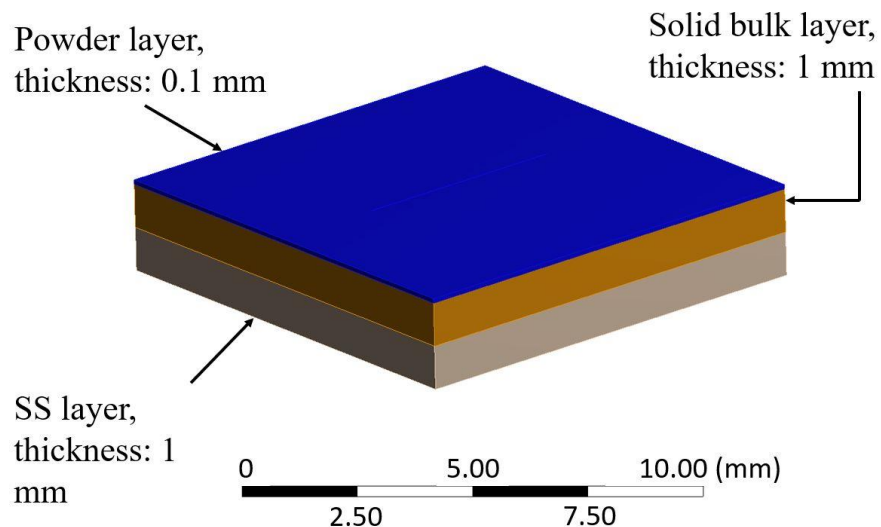


Figure 5.1 Solid model adopted for the transient thermal FE analysis.

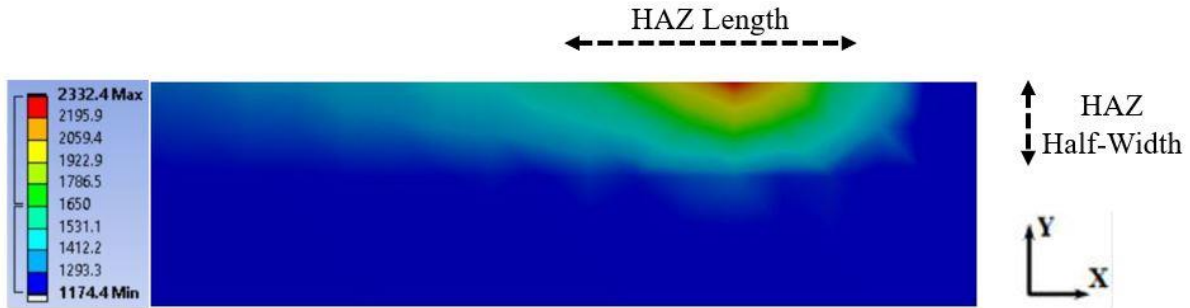


Figure 5.2 Schematic of HAZ width as measured from simulation results.

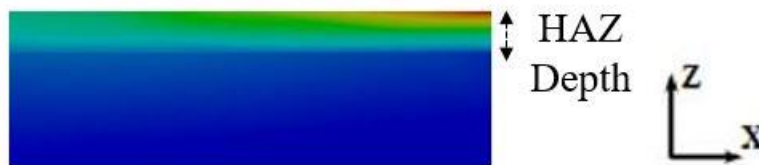


Figure 5.3 Schematic of HAZ depth as measured from simulation results.

velocity of the beam. The line is offset from the edge on the top layer by 2.5 mm to consider the effect of powder bed thermal conductivity. Similar models have presented satisfactory results for the continuum models [79]–[81]. The distance from the build plate does not affect the microstructure and the mechanical properties when above a certain value and the distance of more than 1 mm is acceptable [82], [83]. For various simulations, the temperature profile generated is evaluated to determine the HAZ dimensions as shown in figures 5.2 and 5.3. The results generated are plotted in figure 5.4. As compared to the Ti64 material, the simulations presented a more uniform heat distribution on the top surface, and the trailing tail of the HAZ is shorter when compared with the results [39].

Information about the HAZ was extracted using the above technique. A complete list of the dimensions is presented as appendix 2. The HAZ dimensions are evaluated by measuring the dimension of the contours till the melt temperature of $ZrSi_2$, 1650 °C is measured within the

software. As seen from part (a) of the figure, the effect of beam power has significantly affected the HAZ depth. The minimum HAZ depth is 80 microns at 500 W and 1000 mm/s parameters. Increasing the beam power increases the HAZ depth, and the difference in the depth increases at higher power. The variation in the melt pool width is less with all the values below 0.6 mm for beam power of 500 W and all values around 0.8 mm for beam power of 1000 W.

Higher beam power results in higher HAZ width. It is observed that the effect of increasing the beam power has a more prominent effect as compared to increasing the scanning speed of the electron beam. The HAZ width values will aid in selecting the hatch spacing for future researchers for experimenting with 2D simulations. The overlap is required for the beam scanning path so that proper joint is ensured and a completely dense UHTC part can be manufactured using this process. The images (c) and (d) show the variation in the HAZ dimensions with a variation in the electron beam power. An average increase of 0.25 mm is registered for the increasing beam power at 250 mm/s scanning speed, which reduces to 0.005 mm at 1000 mm/s. This stark difference is not observed for HAZ width, where the average difference of 0.2 mm is maintained even at increasing scanning speeds. These values have been compared with the experimental observations. These

Table 5.1 Constant process parameters for simulating the mathematical model.

Beam spot diameter	4×10^{-4} m
Powder layer thickness	1×10^{-4} m
Solid layer thickness	9×10^{-4} m
Stainless steel thickness	1×10^{-3} m
Accelerating Voltage	60 kV
Preheating temperature	800 °C

simulation results can also be used in evaluating the thermal residual stresses when experimenting with 3D builds, similar to the metal processes [84].

Another interesting observation is the uniformity of the Heat Affected Zone in the FE model simulation at higher scanning speeds. The higher thermal conductivity and diffusivity are responsible for the quicker dissipation of heat in the powder bed and hence the tail appearing in the HAZ behind the electron beam while traveling is smaller. The same results hold for the cooling of the chamber after the build is complete. Thus, the research regarding the generation of thermal residual stresses in Ti64 will not be fully applicable to the manufacture of UHTCs using the EB-PBF process. The difference in the temperature-dependent thermal conductivity is shown in figure 5.5. The sudden peak in the value is due to the transition of the material from solid to liquid. The conductivity in the liquid stage is also lower as compared to the solid stage of ZSZ -30. The reduced thermal conductivity of the powder bed also follows a similar behavior.

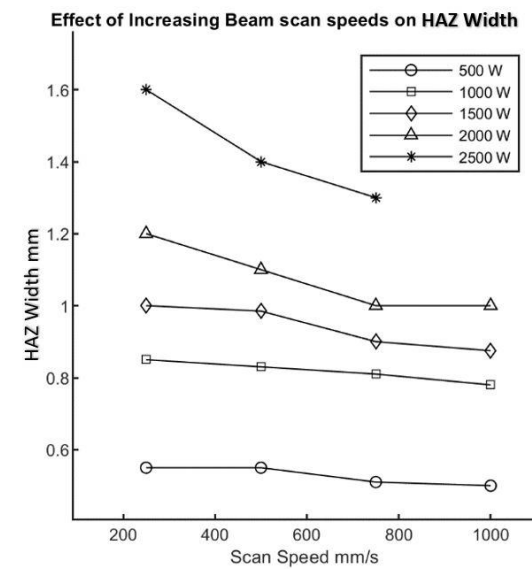
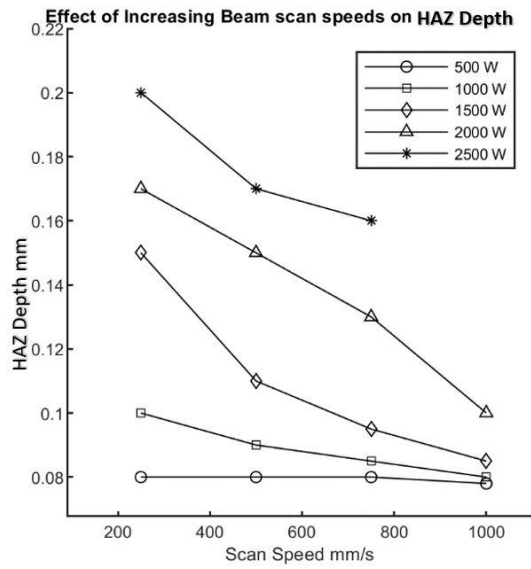
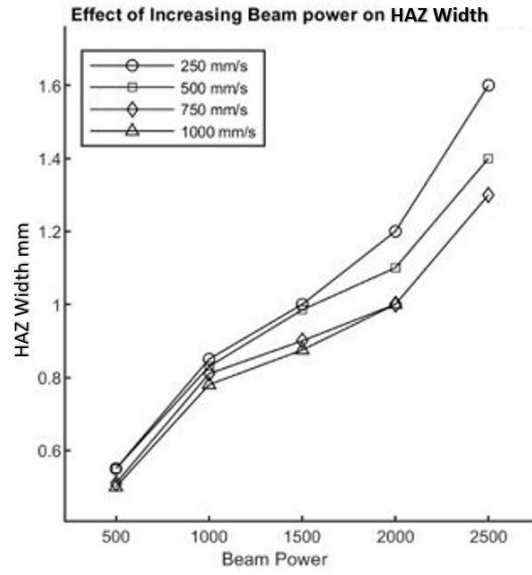
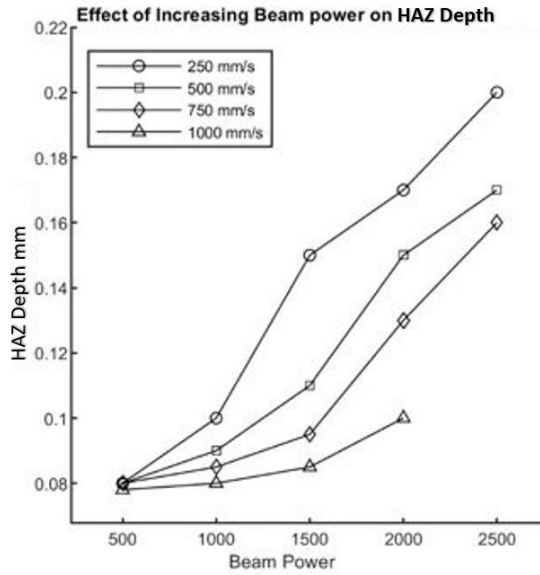


Figure 5.4 Variation of the HAZ dimension with changing process parameters.

- (a) Variation of HAZ depth with increasing beam power.
- (b) Variation of HAZ half-width increasing beam scanning speed.
- (c) Variation of HAZ depth with increasing HAZ depth with increasing beam power.
- (d) Variation of increasing HAZ half-width with increasing beam scanning speed.

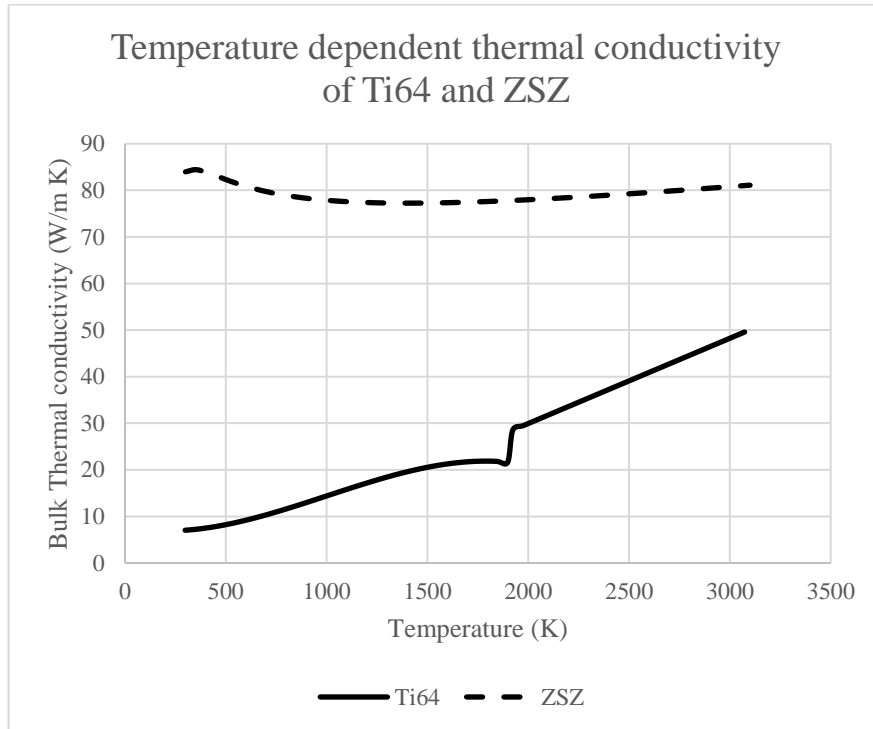


Figure 5.5 Temperature dependent thermal conductivity of Ti64 (based on the work of Neira Arce) and ZSZ, where ZSZ is $ZrB_2 - 30 \text{ vol\% } ZrSi_2$.

5.2 Experimental results

The processed tracks were analyzed for surface roughness and melt consolidation dimensions. Each track was analyzed using the SEM microscope and the Keyence Confocal Laser microscope to assess the quality of the build. The confocal laser microscope images were analyzed to measure the width of the HAZ which will be compared with the experimental results. The surface roughness measured will help in downsizing the parameters. From all the surface roughness values, a maximum of 125 microns is considered for further evaluation, as layer thickness greater than 125 microns is usually not desirable for powder bed processes. Melt Layer thickness is a controlling factor for the mechanical strength of the part and the selection of melt layer thickness also depends on the surface roughness [17].

5.2.1 Experimental track observation

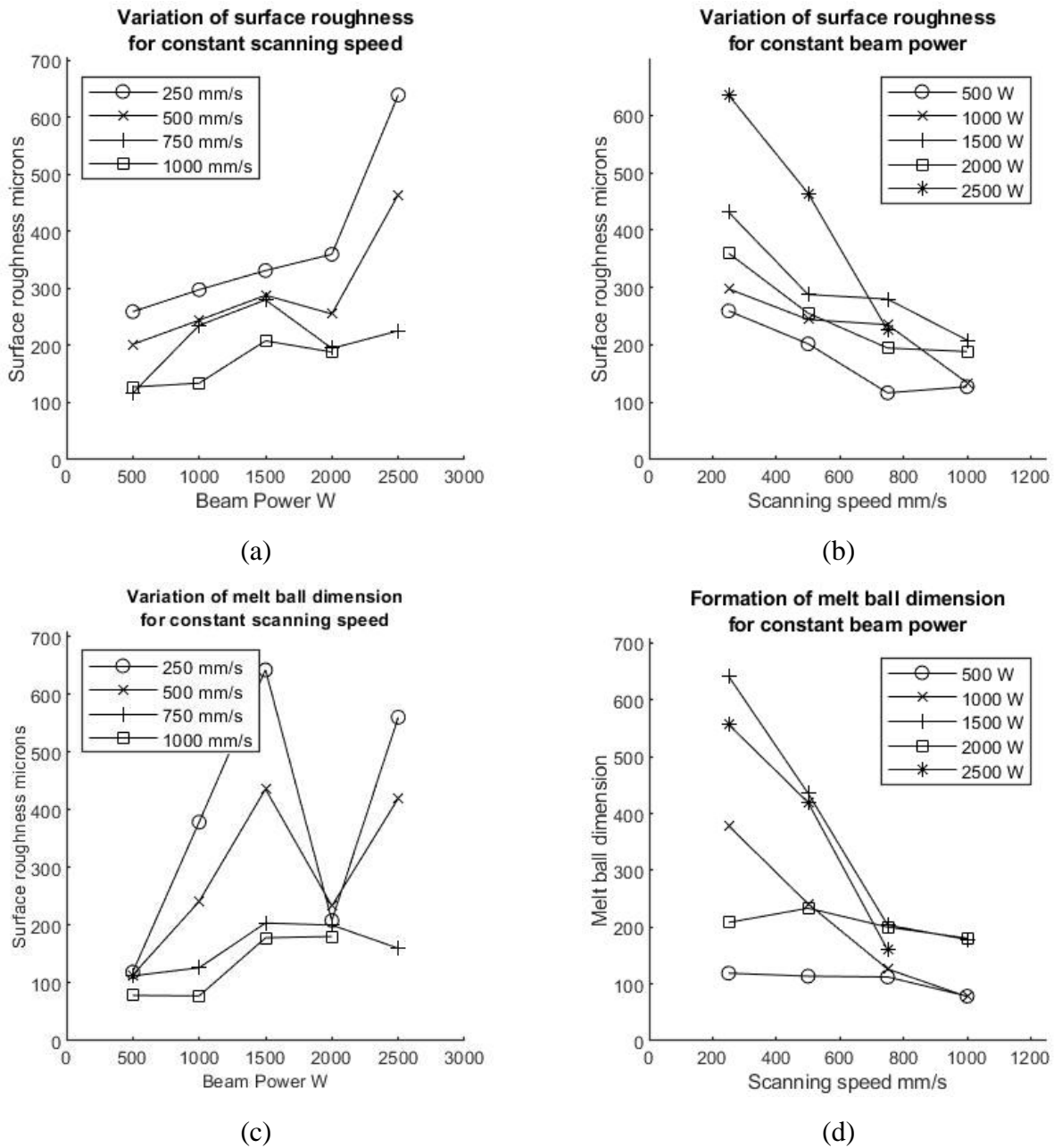


Figure 5.6 Variation of surface roughness and melt consolidation with changing process parameters. (a) Variation surface roughness with increasing beam power (a) and increasing beam scanning speed (b). Variation of melt consolidation with increasing HAZ depth with increasing beam power (c) and with increasing beam scanning speed (d).

The beam diameter in the experiment was set as 400 microns, and the allowable maximum dimension for the melt consolidation is taken as 125 microns, a quarter of the beam diameter. Dimensions higher than this would interfere with the powder spreading rake action, which would highly disrupt the thermal energy transfer in the powder bed. Higher surface roughness and melt ball formations can also cause delamination in the part due to insufficient joining of the layers. The results of the calculations are presented in the following section. In these results, the SEM images are also explored in detail to detect the quality of the melt tracks. The surface roughness and melt consolidation dimensions observed for 1500 W electron beam tracks is higher than what is observed for the 2000 W electron beam power.

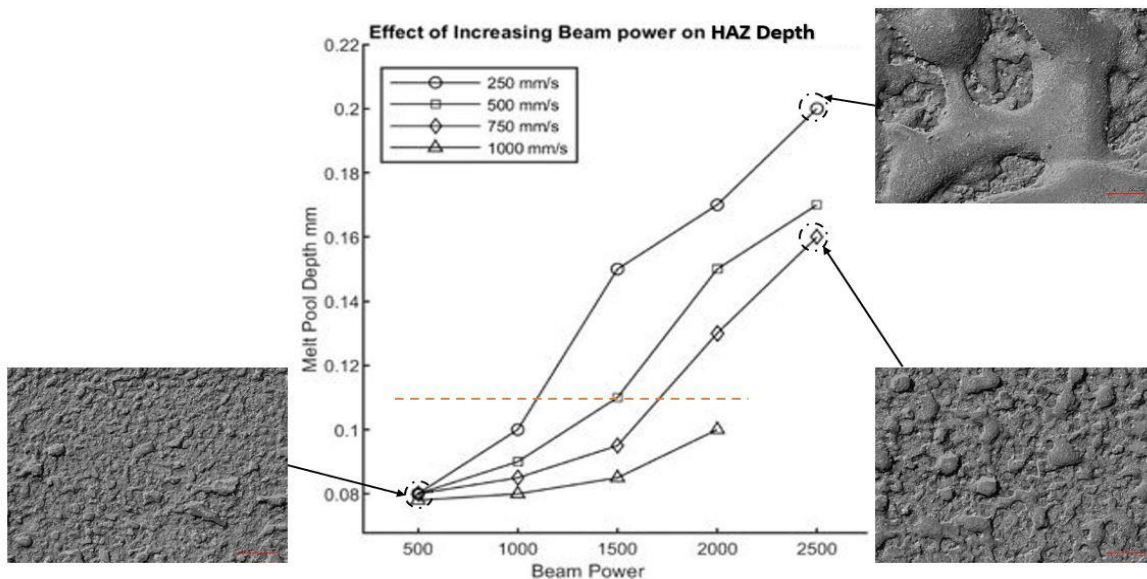
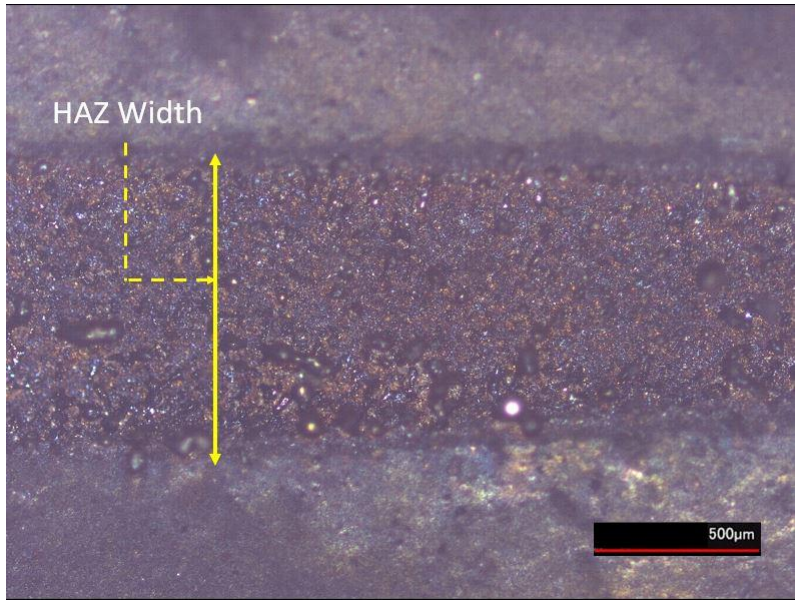


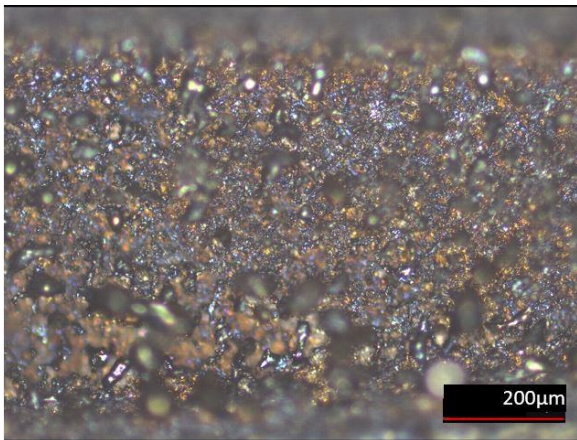
Figure 5.7 Laser microscope images for the mentioned process parameters. (Increased melt consolidation, resulting in large values of surface roughness is observed for higher power and low speeds, as shown in the images on the right side. It was found that when the predicted HAZ depth went higher than 0.1 mm, surface roughness values deemed it unsuitable for the EB-PBF process).

The measured observations are displayed in figure 5.6. Since the starting condition is the prepared pucks with an absence of powder raking action, the surface roughness can be considered to be an outcome of the interaction of the powder and the electron beam only. Higher line energy density has resulted in formation of a network of consolidated material in the track. The SEM of the network structure has revealed an increase in $ZrSi_2$ on the top surface and joining different consolidation regions together. The time duration for heat transfer at any instance is higher than required for a line energy density above 2.5, resulting in melt ball formation which is verified by studying the laser imaging of the melt tracks, as shown in figure 5.7. Above the predicted HAZ depth of 0.1 mm, which is denoted by the dashed orange line, melt consolidation were observed due to higher energy density.

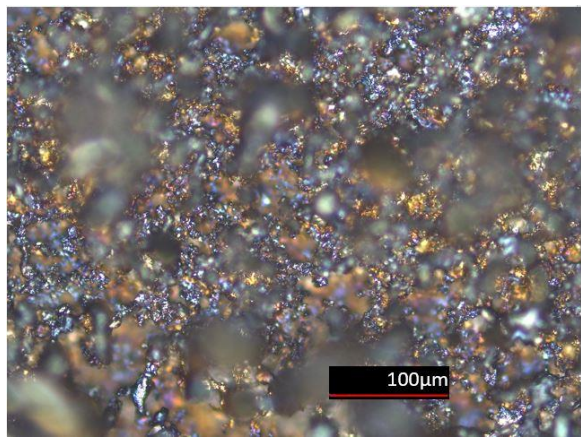
Using the Laser Confocal microscope, magnification of 5x, 10x, and 20x was possible and the same was observed. The images at this magnification helped in determining the width of the HAZ, and the surface roughness of the samples. The feature of generating a C – Laser DIC was useful tool when focusing on the entire view was difficult due to the varying depth of the sample. Such results for sample P1 – Run 1 are given in figure 5.8. Image (a) can be used to determine the HAZ width, as shown in figure and the same is done for all the process tracks. SEM microscopy images were also analyzed. Some of the SEM images are presented in the following figures.



(a)



(b)



(c)

Figure 5.8 Optical imaging of the HAZ tracks on the pucks for 5x (a), 10x (b) and 20x (c) magnification. The images shown are for the first run, Sample P1 – Run1.

The results for each puck are as follows:

- Sample P1

Run 1: The maximum surface roughness is 259 microns. This is much larger than the expected layer thickness of 100 microns. This will cause interference with the next layer and based on this assumption, this observation is rejected. This high surface roughness can be due to the low scanning speed and high line energy density of 2.

Run 2: The maximum surface roughness is 201 microns. This is lower than the previous result but is still double of the desired layer thickness. This observation is also rejected based on the similar reason. The SEM image of this run shows some interesting results, where the $ZrSi_2$ has melted and wetted ZrB_2 particles, and solidified to generate a solid bulk. As can be seen from the images in figure 5.9, melt balls of $ZrSi_2$ are formed in the

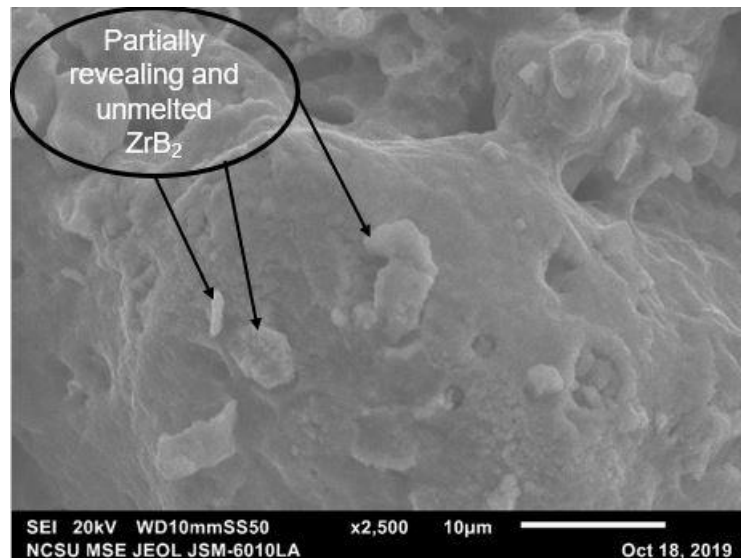


Figure 5.9 Partially and unmelted ZrB_2 particles can be seen engulfed in the melted and solidified $ZrSi_2$. The image is for the process parameter of 500 W beam power and 500 mm/s scanning speed.

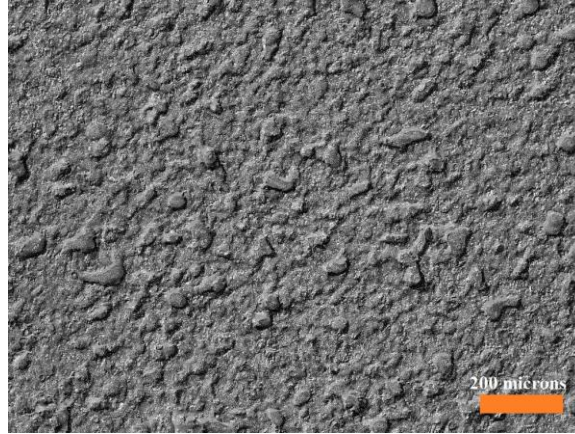


Figure 5.10 Surface texture of the track with the process parameter of 500 W beam

power and 750 mm/s scanning speed with Laser Confocal microscope.

melt track, with even smaller satellite particles detected on the surface. These are the nonmelted particles of ZrB₂.

Run 3: The maximum surface roughness is 103.768 microns. This result is acceptable. However, the melt ball maximum dimension is 112 microns. This is near to the required criteria. The melt consolidations were measured, and the maximum value achieved was 112 microns which is nearly acceptable. Figure 5.10 shows the Laser C – DIC image.

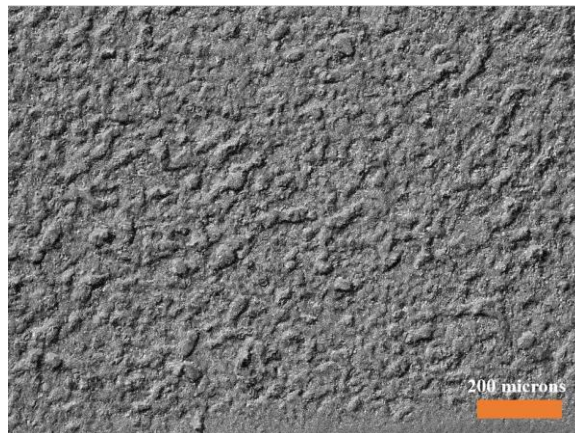


Figure 5.11 Surface texture of the track with the process parameter of 500 W beam

power and 1000 mm/s scanning speed with Laser Confocal microscope.

Run 4: The maximum surface roughness is 90.016 μm , and the HAZ maximum dimension is 78.525 microns. Both the conditions are satisfied by this run and is one of the favourable results of all the parameters. Figure 5.11 shows the Laser C – DIC image

Run 5: The maximum surface roughness is 481.19 microns. Melt ball formations are witnessed with the maximum dimension is 289.56 microns.

Run 6: The maximum surface roughness is 390.31 microns. Melt ball formations are witnessed with the maximum dimension is 312.711.

For runs 5 and 6, the line energy densities are 2.5 and 3. Even for the lower beam power of 250 W and 300 W, which is much lower than the previous 500 W beam power used earlier, melt consolidations are observed. An interesting phenomenon observed is that unlike the metal alloys, individual metal balls are not formed, rather melt consolidations that are interconnected with each other are observed.

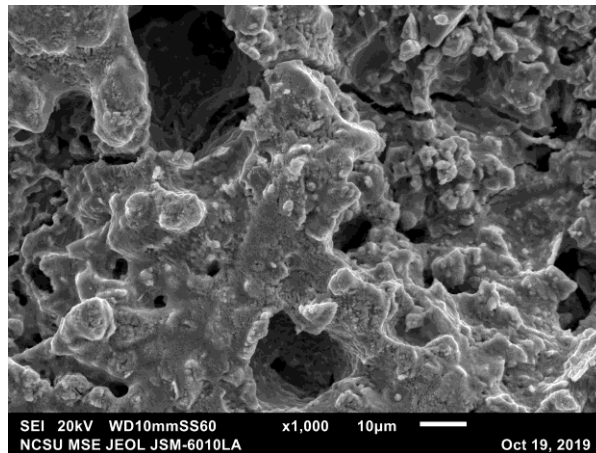


Figure 5.12 SEM image of process parameter 1000 W beam power and 1000 mm/s scanning speed. A network structure of the molten and solidified material is observed in the track.

From the sample puck P1, runs 3 and 4 give the best result and these can be used for future EB-PBF builds of UHTC parts.

- Sample P2:

Run 1: The maximum surface roughness is 297.75 microns. A line energy density of 4 is high for this material and hence the observations were expected.

Run 2: The maximum surface roughness is 244.28 microns. This observation is double of the desired layer thickness. This observation is also rejected based on the similar reason.

Run 3: The maximum surface roughness is 235.31 microns. The maximum melt ball dimensions is 126.334 um which is higher than the predefined maximum allowable value.

Run 4: The maximum surface roughness is 103.561 microns, and the HAZ maximum dimension is 77.61 microns. This process parameter satisfies the rubrics defined earlier and hence is a potential for future application. The SEM image of this track is shown in figure 5.13.

Run 5: The maximum surface roughness is 392.85 microns with a melt consolidation dimension of 208.21 microns. Heavy melt structure is observed for this track with a line density of 8.

Run 6: The maximum surface roughness is 255.36 microns with a melt consolidation dimension of 233.42 microns. The line density for this structure is 4. For the run 2, an interesting phenomenon was observed. The ZrB_2 powder particles were found to recrystallize and reorient in the $ZrSi_2$ pool and the mixture is solidified. Long and thin flakes of similar shape are found and shown in figure 5.14.

- Sample P3

Run 1: The maximum surface roughness is 194.95 microns. The biggest HAZ dimension is 200 um which is almost double of the maximum limit decided by us. Thus, this case is also rejected.

Run 2: The maximum surface roughness is 149.668 um. Even though this observation is near to the decided value of 125um, the biggest HAZ dimension is 180.522 um which is greater than the threshold of 100 um.

Run 3: The maximum surface roughness is 203.491 microns. The maximum melt ball dimension is 160.036 um. Both values are above the limit set by us for selection. Hence, this case is also rejected.

Run 5: The maximum surface roughness is 245.453 um. This result is unacceptable for our study and is not to be analyzed further. Also, the maximum melt ball dimension is 272.141 um which is much higher than the upper cap.

Run 6: The maximum surface roughness is 316.26 um. Even though the beam power is 300 W, which is lower than the 200 W, as for the other samples of P3 and a line scanning density of 2. Hence, the beam power plays a more important role as compared to the beam scanning speed.

- Sample P6

Run 1: The maximum surface roughness is 424.694 microns. This amount is considerably larger than the decided amount of 125 microns. Also, the biggest melt consolidation dimension is 641.804 um which is almost double of the maximum limit decided by us. Thus, this case is also rejected.

Run 2: The maximum surface roughness is 277.728 microns. The biggest HAZ dimension is 435.629 μm which is greater than the threshold of 100 microns. It surpasses both the decided values for the selection criterion.

Run 3: The maximum surface roughness is 260.19 microns. The maximum melt ball dimension is 203.826 microns. Both values are above the limit set by us for selection. Hence, this case is also rejected.

Run 4: The maximum surface roughness is 195.213 microns. The maximum melt ball dimension is 178.151 microns. Both values are above the limit set by us for selection. Hence, this case is also rejected.

Run 5: The maximum surface roughness is 635.564 microns. This result is unacceptable for our study and is not to be analyzed further. Also, the maximum melt ball dimension is 556.958 μm which is much higher than the upper cap.

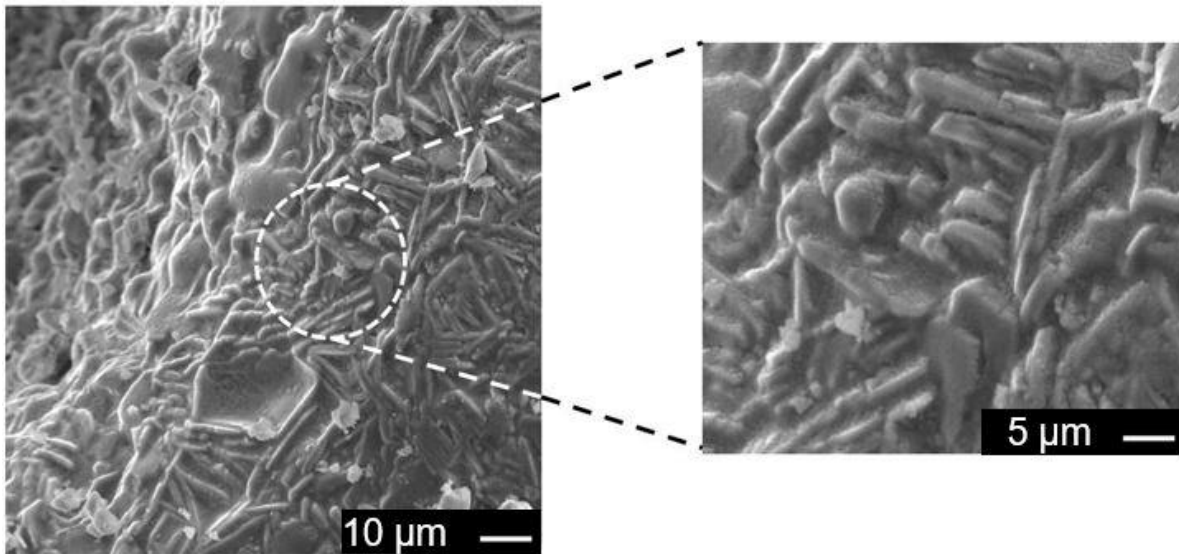


Figure 5.13 SEM image of the process track for sample P2 – Run 4 for electron beam power of 1000 W and scanning speed of 1000 mm/s.

Run 6: The maximum surface roughness is 430.976 microns. This result is unacceptable for our study and is not to be analyzed further. The maximum melt ball dimension is 419.478 μm which is much higher than the upper cap. For all the process parameters in sample P6, none satisfy the predetermined rubrics and hence are not the potential parameters to manufacture UHTC parts using the EB-PBF process.

Final Runs selected:

Based on the above selection criteria, acceptable results are: Sample P1 – Run 3,4; Sample P2 – Run 4; Sample P3 – Run 2; and no parameters of Sample P6.

An interesting result observed for EB-PBF processing of UHTC is the network formation of the melt balls to form melt consolidation instead of individual melt balls as generally seen for metals. Additional SEM images are presented as Appendix 3. Furthermore, EDS calculations on the SEM were done to perform the quantitative analysis of the melt tracks. From the results generated, it

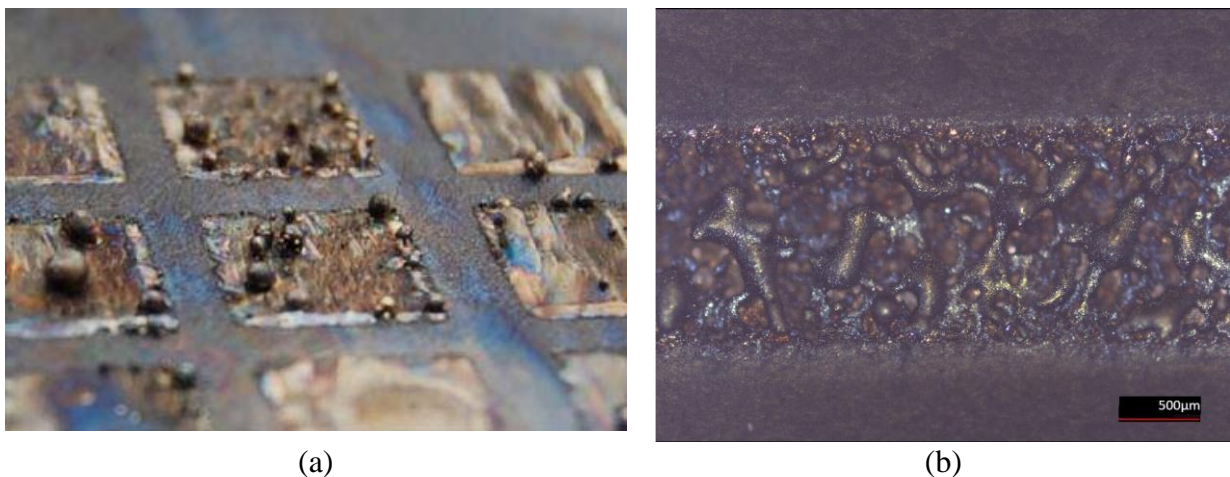


Figure 5.14 Comparison of the top surface texture for metal and UHTC. Separate melt ball formations for Ti-6Al-4V are observed, as published by Zäh and Lutzmann (a) [38].

Connected processed consolidations are observed for $\text{ZrB}_2 - \text{ZrSi}_2$ combination in this

was found that the after Zr, Oxygen was found to have the highest mass percentage followed by Iron, which can be considered as an impurity inclusion in the powder supplied by the supplier.

Surprisingly, Boron was not detected. It was confirmed that with the presence of higher energy elements, it can become difficult to detect Boron, as it has lower levels of energy compared to

Table 5.2 EDS Analysis of all the tracks.

Sample 1	Run1	Run2	Run3	Run4	Run5	Run6
Power (W)	500	500	500	500	250	300
Scan speed(mm/s)	250	500	750	1000	100	100
Line Energy Density	2	1	0.66	0.5	3	2.5
Zr (%)	51.33	46.92	45.12	31.03	31.03	34.92
Si (%)	6.95	9.53	5.75	5.67	5.67	7.44
Sample 2	Run1	Run2	Run3	Run4	Run5	Run6
Power (W)	1000	1000	1000	1000	2000	2000
Scan speed (mm/s)	250	500	750	1000	250	500
Line Energy Density	4	2	1.33	1	8	4
Zr (%)	59.84	49.18	47.28	43.32	53.02	38.42
Si (%)	8.85	8.89	7.46	11.78	7.23	5.74
Sample 3	Run1	Run2	Run3	Run5	Run6	
Power(W)	2000	2000	2500	250	300	
Scan speed (mm/s)	750	1000	750	150	150	
Line Energy Density	2.67	2	3.33	1.67	2	
Zr (%)	61.19	55.11	67.08	70	66.77	
Si (%)	10.13	10.77	11.28	9.13	9.82	

other elements. The trend for other tracks also seems to follow the same trend. Boron cannot be detected in any EDS readings. Various other elements were also detected, like Calcium, Chromium, Manganese and Nickel and Aluminum. The finalized processing conditions are presented in figure 5.15. Process parameters in the shaded region result in a part build of good quality with controlled surface roughness. Using P–V process design charts optimize the selection of process variables to enable robust process outcomes [85].

5.3 Comparison of Simulation and Experimental results

The experimented results provided the viable process parameters for manufacturing $ZrB_2 - 30$ vol% $ZrSi_2$ UHTC using EB-PBF process. The HAZ width measured was compared with the FE simulation results to determine the accuracy of the FE simulation. Figure 5.17 displays the comparison of the results for the process parameters. Maximum difference of 0.1mm, or 15%, is observed in between the two results among all the results. For all the velocities compared, the maximum difference is observed for the 250 mm/s scanning speed, reduced for 500 mm/s and 750

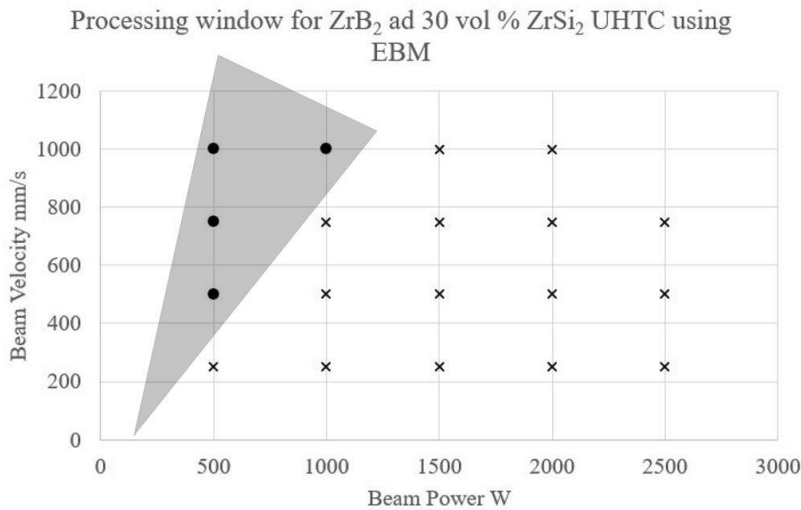


Figure 5.15 Proposed processing window based on the experimental results for manufacturing $ZrB_2 - 30$ vol% $ZrSi_2$ using the EB-PBF process.

mm/s, and becomes negative for 1000 mm/s. This trend in the difference can be pertained to the setup of the FE model analysis. Time stepping of the analysis is a key parameter and the values used in this simulation are compliant with the conditions presented by Jamshidinia et al. [39]. The differences in the result is due to the physical phenomenon like Marangoni convection and capillary effects being ignored. This comparison proves the simulation results and hence promotes the applicability of the same for future experiments. Figure 5.16 shows the HAZ for specimens built with different scanning speeds of 250, 500, 750 and 1000 mm/s and different line energy. The HAZ of parts built with constant scanning speed increases nearly linearly with increasing line energy up to a point, stabilizes and then again increases. The deviation of the mean value increases with increasing line energy. High deviations are caused by an uneven top surface. Generally, at constant line energy the HAZ of the parts increases linearly with scanning speed [86] is observed for Ti-6Al-4V. The minimum HAZ for dense material is 400-450 microns.

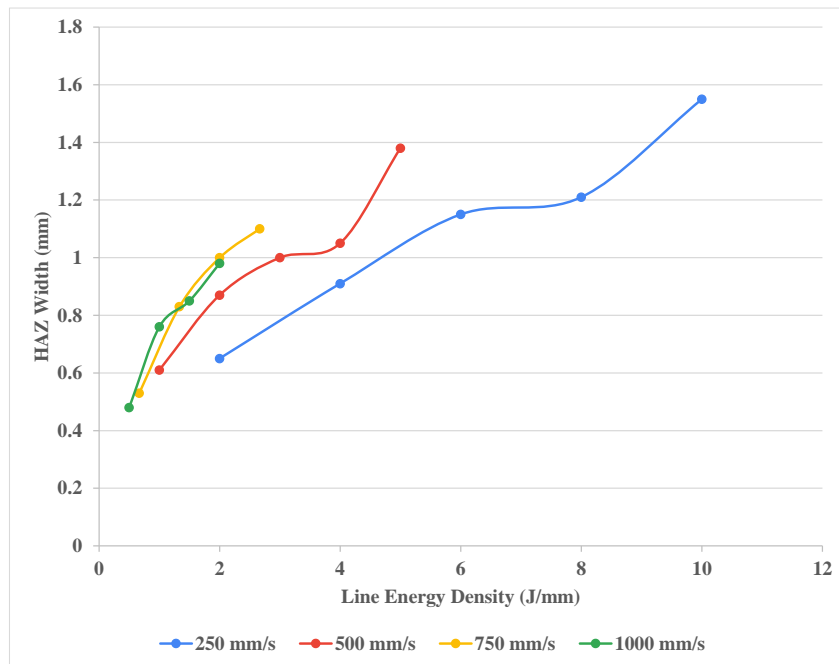


Figure 5.16 Heat-affected Zone of $ZrB_2 - 30 \text{ vol\% } ZrSi_2$ melted by an electron beam with varying scanning speed and line energy.

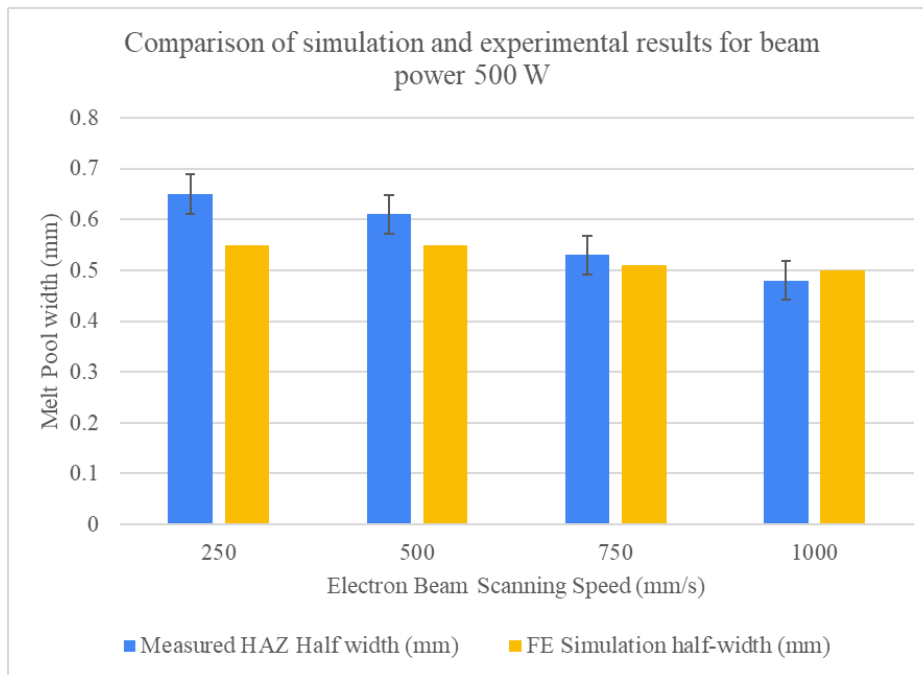


Figure 5.17 Comparison of simulation and experimental results for beam power 500 W.

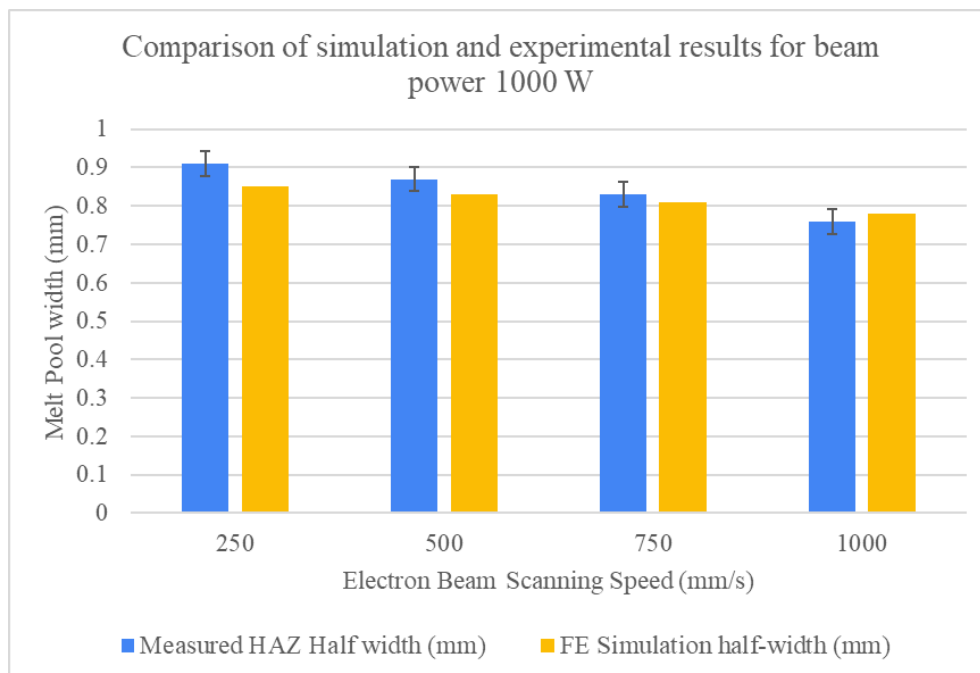


Figure 5.18 Comparison of simulation and experimental results for beam power 1000 W.

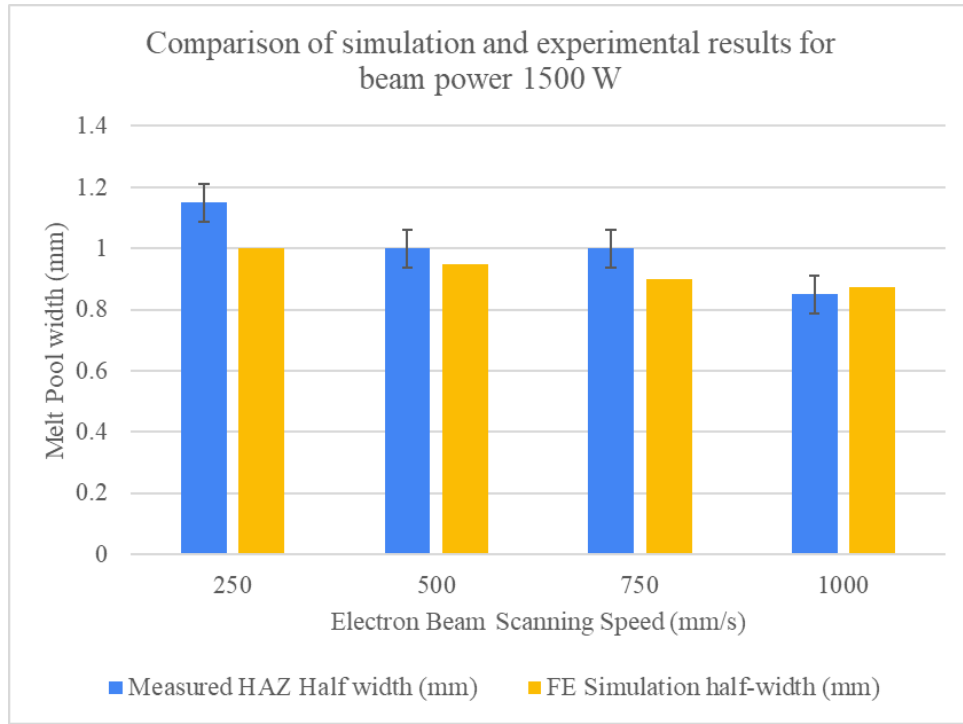


Figure 5.19 Comparison of simulation and experimental results for beam power 1500 W.

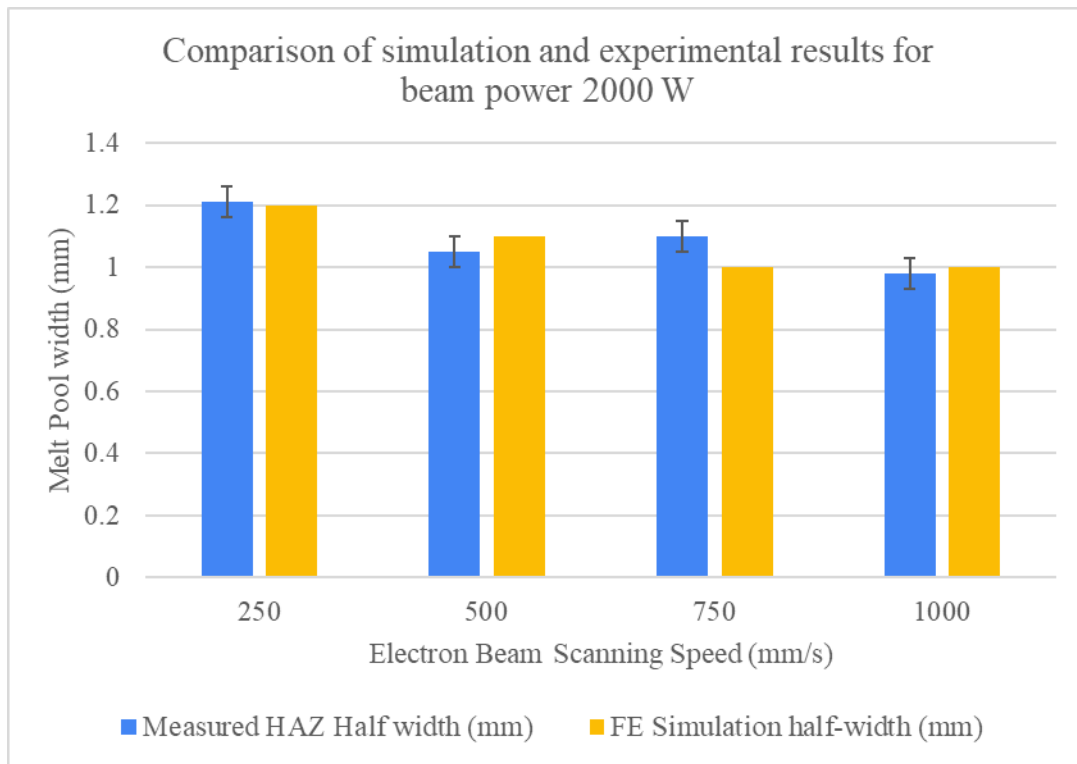


Figure 5.20 Comparison of simulation and experimental results for beam power 2000 W.

CHAPTER 6

CONCLUSION

Ultra-high temperature ceramics have profound potential to be used in environments of thermal extremes given the capability to be manufactured with complex geometries and internal chambers and cavities. Electron Beam Melting process has found insurmountable applicability with aerospace, defence and nuclear applications for manufacturing critical process parts owing to freedom in manufacturing parts with a layer-by-layer process and easy manipulation of the CAD data to generate the machine compatible instructions. In this paper, an effort was made to adapt the EB-PBF process for manufacturing UHTC of $ZrB_2 - 30 \text{ vol\% } ZrSi_2$ combination. A mathematical model was developed with the material properties of the above-mentioned combinations and potential process parameters were determined. Standard heat transfer equations were solved, and the electron beam heat source values were rectified based on the literature review and applied as a distribution over the applied zone. The parameters were experimented with Arcam S12 EB-PBF machine and the results were analysed with Laser Confocal microscope and SEM. Assessment criteria for the tracks were defined and the process parameters that abided by the rubric threshold values were reported. The HAZ dimensions were compared with the values generated by simulating the mathematical model and the findings have been presented in the paper. The simulation results concurred with the experimentation results.

The availability of joint-free UHTC parts with complex geometries will promote optimized design realization with lower material weight going into the final product with minimal finishing operations. The research findings will greatly benefit the future development of ZrB_2 parts using EB-PBF and powder bed fusion processes for use in thermal extreme environments, such as

hypersonic flights and friction stir welding. Heating treating the processed part for an extended amount of time will lead to an increase in the density due to sintering which will improve the mechanical property of the part, and hence combine the advantages of complex design feasibility of Additive Manufacturing and near dense part production due to sintering.

The feasibility of manufacturing UHTC using EB-PBF process was experimented. Numerous positive results were observed. The powder did not smoke on interacting with the electron beam, which is a matter of concern due to the damage it does to the machine tool and the electron gun. The experiments proved the formation of molten and solidified tracks, with defects including insufficient melting and melt ball formations. Satisfactory results were obtained for a few process parameter combinations. However, a few challenges are yet to be tackled. In this model, the combination of the two materials has been processed considering the combined properties applied to a single material in the model. Complex physical phenomenon like Marangoni convection, viscous effects, surface tension of the HAZ, molten material fluid flow, etc. have been ignored. The inclusion of these parameters is computationally heavy and expensive and requires high performance computing facilities.

The experimentation of the 1D tracks prove the feasibility of manufacturing UHTCs with EB-PBF process. However, experiment for a 3D part needs to be conducted to understand the complications arising during the process. Numerous other factors like flowability, rake action, scanning strategies, hatch spacing, contour hatching, variable scanning speeds in the part, overhang, etc. play a significant role in the quality of the final part. The Finite Element Analysis model was verified with experimented results.

REFERENCES

- [1] W. G. Fahrenholtz, E. J. Wuchina, W. E. Lee, and Y. Zhou, *Ultra-high temperature ceramics: materials for extreme environment applications*. John Wiley & Sons, 2014.
- [2] L. Kaufman and E. V. Clougherty, “Investigation of boride compounds for very high temperature applications (Technical Documentary Report No. RTD-TDR-63-4096),” p. Part 1, 1963.
- [3] S. M. Johnson, “Ultra High Temperature Ceramics UHTCs,” 2015.
- [4] D. D. Jayaseelan, Y. Xin, and L. Vandeperre, “Development of Multi-Layered Thermal Protection System (TPS) for Aerospace Applications,” *Compos. Part B*, vol. 79, pp. 392–405, 2015.
- [5] W. A. McConarty and F. M. Anthony, “Design and evaluation of active cooling systems for Mach 6 cruise vehicle wings,” 1971.
- [6] H. T. Airframe, “Return To Design of a Convective Cooling System for a Mach 6,” no. December 1971, 2020.
- [7] N. P. Bansal, *Handbook of Ceramic Composites.*, no. Vol. 200. Springer, 2005.
- [8] D. D. Jayaseelan, S. Venugopal, A. Heaton, and P. M. Brown, “UHTC composites for hypersonic applications,” 2012.
- [9] ASTM International, “F2792-12a - Standard Terminology for Additive Manufacturing Technologies,” *Rapid Manuf. Assoc.*, pp. 10–12, 2013.
- [10] S. Ford and M. Despeisse, “Additive manufacturing and sustainability: an exploratory study of the advantages and challenges,” *J. Clean. Prod.*, vol. 137, pp. 1573–1587, 2016.
- [11] T. J. Horn and O. L. A. Harrysson, “Overview of Current Additive Manufacturing Technologies and Selected Applications,” *Sci. Prog.* (, vol. 95, no. 3, pp. 255–282, 2012.

- [12] R. Jiang, R. Kleer, and F. T. Piller, "Predicting the Future of Additive Manufacturing: A Delphi Study on Economic and Societal Implications of 3D Printing for 2030," *Technol. Forecast. Soc. Chang.*, vol. 117, pp. 84–97, 2017.
- [13] A. Busachi, J. Erkoyuncu, and P. Colegrove, "A Review of Additive Manufacturing Technology and Cost Estimation Techniques for the Defence Sector," *CIRP J. Manuf. Sci. Technol.*, vol. 19, pp. 117–128, 2017.
- [14] A. Busachi, J. Erkoyuncu, P. Colegrove, R. Drake, C. Watts, and F. Martina, "Defining Next-Generation Additive Manufacturing Applications for the Ministry of Defence (MoD)," *Procedia CIRP*, vol. 55, pp. 302–307, 2016.
- [15] V. Petrovic, V. H. Gonzalez, and O. J. Jordá Ferrando, "Additive Layered Manufacturing: Sectors of Industrial Application shown through Case Studies," *Int. J. Prod. Res.*, vol. 49, no. 4, pp. 1061–1079, 2011.
- [16] M. E. Orme *et al.*, "Additive manufacturing of lightweight, optimized, metallic components suitable for space flight," *J. Spacecr. Rockets*, vol. 54, no. 5, pp. 1050–1059, 2017.
- [17] J. K. Algardh *et al.*, "Thickness dependency of mechanical properties for thin-walled titanium parts manufactured by Electron Beam Melting (EBM) ®," *Additive Manufacturing*, vol. 12, pp. 45–50, 2016.
- [18] M. Bernhard, "Additive Manufacturing Technologies – Rapid Prototyping to Direct Digital Manufacturing," *Assem. Autom.*, vol. 32, no. 2, Jan. 2012.
- [19] L. Facchini, E. Magalini, P. Robotti, and A. Molinari, "Microstructure and mechanical properties of Ti-6Al-4V produced by electron beam melting of pre-alloyed powders," *Rapid Prototyp. J.*, vol. 15, no. 3, pp. 171–178, 2009.

- [20] M. Attaran, “The Rise of 3-D Printing: The Advantages of Additive Manufacturing Over Traditional Manufacturing,” *Bus. Horiz.*, vol. 60, no. 5, pp. 677–688, 2017.
- [21] T. Pereira, J. V. Kennedy, and J. Potgieter, “A comparison of traditional manufacturing vs additive manufacturing, the best method for the job,” *Procedia Manuf.*, vol. 30, pp. 11–18, 2019.
- [22] X. Gong, T. Anderson, and K. Chou, “Review on Powder-Based Electron Beam Additive Manufacturing Technology,” *Manuf. Rev.*, vol. 1, 2014.
- [23] C. Körner, “Additive manufacturing of metallic components by selective electron beam melting - A review,” *International Materials Reviews*, vol. 61, no. 5. Taylor and Francis Ltd., pp. 361–377, 2016.
- [24] L. Portolés, O. Jordá, and L. Jordá, “A Qualification Procedure to Manufacture and Repair Aerospace Parts with Electron Beam Melting,” *J. Manuf. Syst.*, vol. 41, pp. 65–75, 2016.
- [25] M. Galati and L. Iuliano, “A Literature Review of Powder-Based Electron Beam Melting Focusing on Numerical Simulations,” *Addit. Manuf.*, vol. 19, pp. 1–20, 2018.
- [26] P. Drescher, M. Sarhan, and H. Seitz, “An investigation of sintering parameters on titanium powder for electron beam melting processing optimization,” *Materials (Basel)*, vol. 9, no. 12, 2016.
- [27] T. R. Mahale, *Electron beam melting of advanced materials and structures*. North Carolina State University, 2009.
- [28] S. Tammam-Williams, H. Zhao, F. Léonard, F. Derguti, I. Todd, and P. B. Prangnell, “XCT analysis of the influence of melt strategies on defect population in Ti-6Al-4V components manufactured by Selective Electron Beam Melting,” *Mater. Charact.*, vol. 102, pp. 47–61, 2015.

- [29] N. Raghavan *et al.*, “Numerical modeling of heat-transfer and the influence of process parameters on tailoring the grain morphology of IN718 in electron beam additive manufacturing,” *Acta Mater.*, vol. 112, pp. 303–314, 2016.
- [30] M. Markl and C. Körner, “Powder layer deposition algorithm for additive manufacturing simulations,” *Powder Technol.*, vol. 330, pp. 125–136, 2018.
- [31] C. Körner, E. Attar, and P. Heintl, “Mesoscopic simulation of selective beam melting processes,” *J. Mater. Process. Technol.*, vol. 211, no. 6, pp. 978–987, 2011.
- [32] R. Ammer, U. Rüde, M. Markl, and C. Körner, “Modeling of Thermodynamic Phenomena with Lattice Boltzmann Method for Additive Manufacturing Processes,” 2017.
- [33] W. Yan, Y. Qian, W. Ma, B. Zhou, Y. Shen, and F. Lin, “Modeling and Experimental Validation of the Electron Beam Selective Melting Process,” *Engineering*, vol. 3, no. 5, pp. 701–707, 2017.
- [34] H. B. Qi, Y. N. Yan, F. Lin, and R. J. Zhang, “Scanning method of filling lines in electron beam selective melting,” *Proc. Inst. Mech. Eng. Part B J. Eng. Manuf.*, vol. 221, no. 12, pp. 1685–1694, 2007.
- [35] A. Neira-Arce and others, “Thermal Modeling and Simulation of Electron Beam Melting for Rapid Prototyping on Ti6Al4V Alloys.,” 2012.
- [36] M. Z"ah and S. Lutzmann, “Modelling and Simulation of Electron Beam Melting,” *Prod. Eng.*, vol. 4, no. 1, pp. 15–23, 2010.
- [37] M. Galati, L. Iuliano, A. Salmi, and E. Atzeni, “Modelling energy source and powder properties for the development of a thermal FE model of the EBM additive manufacturing process,” *Addit. Manuf.*, vol. 14, pp. 49–59, 2017.
- [38] B. Cheng and K. Chou, “A Numerical Investigation of Thermal Property Effects on Melt

- Pool Characteristics in Powder-Bed Electron Beam Additive Manufacturing,” in *Proceedings of the Institution of Mechanical Engineers*, 2018, pp. 1615–1627.
- [39] M. Jamshidinia, F. Kong, and R. Kovacevic, “Numerical modeling of heat distribution in the electron beam melting of Ti-6Al-4V,” *J. Manuf. Sci. Eng. Trans. ASME*, vol. 135, no. 6, pp. 1–14, 2013.
- [40] P. R. Carriere, “Energy and Charge Transfer during Electron Beam Melting,” pp. 1–258, 2018.
- [41] C. Sun, M. C. Gupta, and K. M. B. Taminger, “Electron Beam Sintering of Zirconium Diboride,” *J. Am. Ceram. Soc.*, vol. 93, p. 9, 2010.
- [42] F. Monteverde, “Beneficial effects of an ultra-fine α -SiC incorporation on the sinterability and mechanical properties of ZrB₂,” *Appl. Phys. A Mater. Sci. Process.*, vol. 82, no. 2, pp. 329–337, 2006.
- [43] E. Wuchina, E. Opila, M. Opeka, W. Fahrenholtz, and I. Talmy, “UHTCs: Ultra-High Temperature Ceramic materials for extreme environment applications,” *Electrochem. Soc. Interface*, vol. 16, no. 4, pp. 30–36, 2007.
- [44] M. Ahmad, G. Ali, E. Ahmed, M. A. Haq, and J. I. Akhter, “Novel microstructural growth in the surface of Inconel 625 by the addition of SiC under electron beam melting,” *Appl. Surf. Sci.*, vol. 257, no. 17, pp. 7405–7410, 2011.
- [45] M. Ahmad, J. I. Akhter, G. Ali, and M. Akhter, “In-situ synthesis of oxygen free SiC fibers and ropes by electron beam melting,” *Mater. Lett.*, vol. 61, no. 4–5, pp. 956–959, 2007.
- [46] Y. Ivanov *et al.*, “Multilevel hierarchical structure formed in the film (Ti)/substrate (SiC-ceramics) system under irradiation by an intense pulsed electron beam,” *AIP Conf. Proc.*,

- vol. 2051, 2018.
- [47] R. He, D. Fang, and P. Wang, "Electrical Properties of ZrB₂--SiC Ceramics with Potential for Heating Element Applications," *Ceram. Int.*, vol. 40, no. 7, pp. 9549–9553, 2014.
- [48] M. Mallik, A. J. Kailath, K. K. Ray, and R. Mitra, "Electrical and thermophysical properties of ZrB₂ and HfB₂ based composites," *J. Eur. Ceram. Soc.*, vol. 32, no. 10, pp. 2545–2555, 2012.
- [49] S. Guo, Y. Kagawa, and T. Nishimura, "Mechanical Behavior of Two-Step Hot-Pressed ZrB₂-Based Composites with ZrSi₂," *J. Eur. Ceram. Soc.*, vol. 29, no. 4, pp. 787–794, 2009.
- [50] S. Guo, T. Nishimura, and Y. Kagawa, "Low-Temperature Hot Pressing of ZrB₂-Based Ceramics with ZrSi₂ Additives," *Int. J. Appl. Ceram. Technol.*, vol. 8, no. 6, pp. 1425–1435, 2011.
- [51] J. J. Sha, Z. Q. Wei, and J. Li, "Mechanical Properties and Toughening Mechanism of WC-Doped ZrB₂--ZrSi₂ Ceramic Composites by Hot Pressing," *Mater. Des.*, vol. 62, pp. 199–204, 2014.
- [52] J. J. Sha, J. Li, and Y. C. Wang, "Toughening Effect of Short Carbon Fibers in the ZrB₂--ZrSi₂ Ceramic Composites," *Mater. Des.*, vol. 75, pp. 160–165, 2015.
- [53] M. Setton and J. Van Der Spiegel, "Structural and electrical properties of ZrSi₂ and Zr₂CuSi₄ formed by rapid thermal processing," *J. Appl. Phys.*, vol. 70, no. 1, pp. 193–197, 1991.
- [54] S. Guo, "Densification of ZrB₂-Based Composites and their Mechanical and Physical Properties: A Review," *J. Eur. Ceram. Soc.*, vol. 29, no. 6, pp. 995–1011, 2009.
- [55] G. Welsch, R. Boyer, and E. W. Collings, *Materials properties handbook: titanium alloys*.

- ASM international, 1993.
- [56] G. S. Upadhyaya, *Powder metallurgy technology*. Cambridge Int Science Publishing, 1997.
- [57] R. M. German, "Powder metallurgy science," *Met. Powder Ind. Fed. 105 Coll. Rd. E, Princeton, N. J. 08540, U. S. A, 1984. 279*, 1984.
- [58] G. B. J. de Boer, C. de Weerd, D. Thoenes, and H. W. J. Goossens, "Laser Diffraction Spectrometry: Fraunhofer Diffraction Versus Mie Scattering," *Part. Part. Syst. Charact.*, vol. 4, no. 1–4, pp. 14–19, 1987.
- [59] A. Koptyug, M. Bäckström, C. A. Botero Vega, V. Popov, and E. Chudinova, "Developing new materials for electron beam melting: Experiences and challenges," *Mater. Sci. Forum*, vol. 941 MSF, no. December, pp. 2190–2195, 2018.
- [60] J. W. Zimmermann, G. E. Hilmas, W. G. Fahrenholtz, R. B. Dinwiddie, W. D. Porter, and H. Wang, "Thermophysical properties of ZrB₂ and ZrB₂-SiC ceramics," *J. Am. Ceram. Soc.*, vol. 91, no. 5, pp. 1405–1411, 2008.
- [61] D. L. McClane, "Thermal properties of zirconium diboride - transition metal boride solid solutions," 2014.
- [62] Y. S. Touloukian and C. Y. Ho, "Thermal conductivity. Nonmetallic solids," *Thermophys. Prop. matter-The TPRC Data Ser. New York IFI/Plenum, 1970-*, Ed. by Touloukian, YS/ e (series ed.); Ho, CY/ e (series tech. ed.), 1970.
- [63] M. W. Chase Jr, "NIST-JANAF thermochemical tables," *J. Phys. Chem. Ref. Data, Monogr.*, vol. 9, 1998.
- [64] F. Nakamori, Y. Ohishi, H. Muta, K. Kurosaki, K. I. Fukumoto, and S. Yamanaka, "Mechanical and thermal properties of bulk ZrB₂," *J. Nucl. Mater.*, vol. 467, pp. 612–617,

- 2015.
- [65] S. S. Sih and J. W. Barlow, "The prediction of the emissivity and thermal conductivity of powder beds," *Part. Sci. Technol.*, vol. 22, no. 4, pp. 427–440, 2004.
- [66] G. V. Samsonov, N. F. Podgrushko, M. I. Lesnaya, L. A. Dvorina, and N. F. Selivanova, "Physical properties of group IV transition-metal silicides," *Sov. Phys. J.*, vol. 18, no. 9, pp. 1276–1280, 1975.
- [67] J. Romano, L. Ladani, and J. Razmi, "Temperature Distribution and Melt Geometry in Laser and Electron-Beam Melting Processes -- A Comparison among Common Materials," *Addit. Manuf.*, vol. 8, pp. 1–11, 2015.
- [68] E. Tsotsas, "M7 Heat and Mass Transfer in Packed Beds with Fluid Flow," in *VDI Heat Atlas*, Berlin, Heidelberg: Springer Berlin Heidelberg, 2010, pp. 1327–1342.
- [69] L. Dong, A. Makradi, S. Ahzi, and Y. Remond, "Three-dimensional transient finite element analysis of the selective laser sintering process," *J. Mater. Process. Technol.*, vol. 209, no. 2, pp. 700–706, 2009.
- [70] N. K. Tolochko, M. K. Arshinov, A. V. Gusarov, V. I. Titov, T. Laoui, and L. Froyen, "Mechanisms of selective laser sintering and heat transfer in Ti powder," *Rapid Prototyp. J.*, vol. 9, no. 5, pp. 314–326, 2003.
- [71] M. Neubronner *et al.*, "D6 Properties of Solids and Solid Materials," in *VDI Heat Atlas*, Berlin, Heidelberg: Springer Berlin Heidelberg, 2010, pp. 551–614.
- [72] M. F. Watkins, Y. N. Chilamkurti, and R. D. Gould, "Analytic Modeling of Heat Transfer to Vertical Dense Granular Flows," *J. Heat Transfer*, vol. 142, no. 2, pp. 1–11, 2020.
- [73] J. Goldak, A. Chakravarti, and M. Bibby, "A new finite element model for welding heat sources," *Metall. Trans. B*, vol. 15, no. 2, pp. 299–305, 1984.

- [74] D. Rosenthal, "Mathematical theory of heat distribution during welding and cutting," *Weld. J.*, vol. 20, pp. 220–234, 1941.
- [75] E. Friedman, "Thermomechanical Analysis of the Welding Process Using the Finite Element Method.," *Am. Soc. Mech. Eng.*, no. 75-PVP-27, 1975.
- [76] W. Yan, J. Smith, W. Ge, F. Lin, and W. K. Liu, "Multiscale modeling of electron beam and substrate interaction: a new heat source model," *Comput. Mech.*, vol. 56, no. 2, pp. 265–276, 2015.
- [77] P. Bajaj, J. Wright, I. Todd, and E. A. Jäggle, "Predictive process parameter selection for Selective Laser Melting Manufacturing: Applications to high thermal conductivity alloys," *Addit. Manuf.*, vol. 27, no. December 2018, pp. 246–258, 2019.
- [78] X. Ding, Y. Koizumi, and D. Wei, "Effect of Process Parameters on Melt Pool Geometry and Microstructure Development for Electron Beam Melting of IN718: A Systematic Single Bead Analysis Study," *Addit. Manuf.*, vol. 26, pp. 215–226, 2019.
- [79] D. Riedlbauer, P. Steinmann, and J. Mergheim, "Thermomechanical finite element simulations of selective electron beam melting processes: Performance considerations," *Comput. Mech.*, vol. 54, no. 1, pp. 109–122, 2014.
- [80] P. Michaleris, "Modeling metal deposition in heat transfer analyses of additive manufacturing processes," *Finite Elem. Anal. Des.*, vol. 86, pp. 51–60, 2014.
- [81] J. Cao, M. A. Gharghour, and P. Nash, "Finite-element analysis and experimental validation of thermal residual stress and distortion in electron beam additive manufactured Ti-6Al-4V build plates," *J. Mater. Process. Technol.*, vol. 237, pp. 409–419, 2016.
- [82] N. Hrabe and T. Quinn, "Effects of processing on microstructure and mechanical properties of a titanium alloy (Ti-6Al-4V) fabricated using electron beam melting

- (EBM), part 1: Distance from build plate and part size,” *Mater. Sci. Eng. A*, vol. 573, pp. 264–270, 2013.
- [83] N. Hrabe and T. Quinn, “Effects of processing on microstructure and mechanical properties of a titanium alloy (Ti–6Al–4V) fabricated using electron beam melting (EBM), Part 2: Energy input, orientation, and location,” *Mater. Sci. Eng. A*, vol. 573, pp. 271–277, 2013.
- [84] P. Prabhakar, W. J. Sames, R. Dehoff, and S. S. Babu, “Computational modeling of residual stress formation during the electron beam melting process for Inconel 718,” *Addit. Manuf.*, vol. 7, pp. 83–91, 2015.
- [85] D. R. Clymer, J. Cagan, and J. Beuth, “Power-velocity process design charts for powder bed additive manufacturing,” *J. Mech. Des. Trans. ASME*, vol. 139, no. 10, pp. 1–7, 2017.
- [86] V. Juechter, T. Scharowsky, R. F. Singer, and C. Körner, “Processing window and evaporation phenomena for Ti-6Al-4V produced by selective electron beam melting,” *Acta Mater.*, vol. 76, pp. 252–258, 2014.

APPENDICES

Appendix 1 – Table of electrical resistivities of all the ceramics considered as additive

<u>Material</u>	<u>Melting Point (°C)</u>	<u>Electrical resistivity (ohm-cm)</u>
Ti6Al4V (M)	1660	1.78E-04
SS 316L (M)	1440	7.40E-06
H13 Tool Steel (M)	1427	5.20E-05
Inconel 718 (M)	1336	1.25E-04
Copper (M)	1085	1.68E-06
ASTM F75 CoCr (M)	1330	8.40E-05
Al ₂ O ₃	2322	1.00E+15
BeO	2725	1.00E+14
MgO	3098	1.00E+15
3Al ₂ O ₃ .2SiO ₂	1810	1.05E+02
SiO ₂	1978	1.00E+13
TiO ₂	2113	1.00E+10
ZrO ₂	2715	1.00E+09
AlN	2475	1.00E+13
BN	3000	1.00E+13
Si ₃ N ₄	1878	1.00E+15
HfN	3385	3.30E-05
ZrN	2980	1.36E-05
TiN	2930	2.20E-05
B ₄ C	2720	8.00E-01
HfC	3900	1.09E-04
ZrC	3532	7.00E-05
WC	2870	1.00E-06
SiC	2730	150
HfB ₂	3250	1.20E-05
TiB ₂	3253	2.84E-05
ZrB ₂	3000	9.20E-06

TiB ₂	3253	1.50E-05
MoSi ₂	2230	3.50E-07
ZrSi ₂	1620	4.00E-07

Where (M) denotes metal alloy and its values are presented for reference purposes only.

Appendix 2 – HAZ Dimensions observed from the FEA model simulation & experimentation

Puck No.	Track no.	Beam power (W)	Beam Velocity (mm/s)	Measured HAZ Half width (mm)	FEA simulation Depth (mm)	FEA Simulation half-width (mm)
1	1	500	250	0.65	0.08	0.55
	2	500	500	0.61	0.08	0.55
	3	500	750	0.53	0.08	0.51
	4	500	1000	0.48	0.078	0.5
	5	250	100	0.49	0.08	0.45
	6	300	100	0.55	0.075	0.5
2	1	1000	250	0.91	0.1	0.85
	2	1000	500	0.87	0.09	0.83
	3	1000	750	0.83	0.085	0.81
	4	1000	1000	0.76	0.08	0.78
	5	2000	250	1.21	0.17	1.2
	6	2000	500	1.05	0.15	1.1
3	1	2000	750	1.1	0.13	1
	2	2000	1000	0.98	0.1	1
	3	2500	750	>2	0.16	1.3
	5	250	150	0.5	0.075	0.45
	6	300	150	0.52	0.085	0.45
6	1	1500	250	1.15	0.15	1
	2	1500	500	1	0.11	0.95
	3	1500	750	1	0.09	0.9
	4	1500	1000	0.85	0.085	0.875
	5	2500	250	1.55	0.2	1.6
	6	2500	500	1.38	0.17	1.4